OC6 Project Phase III: Validation of the Aerodynamic Loading on a Wind Turbine Rotor Undergoing Large Motion Caused by a Floating Support Structure

Roger Bergua[1], Amy Robertson[1], Jason Jonkman[1], Emmanuel Branlard[1], Alessandro Fontanella[2], Marco Belloli[2], Paolo Schito[2], Alberto Zasso[2], Giacomo Persico[3], Andrea Sanvito[3], Ervin Amet[4], Cédric Brun[5], Guillén Campaña-Alonso[6], Raquel Martín-San-Román[6], Ruolin Cai[7], Jifeng Cai[7], Quan Qian[8], Wen Maoshi[8], Alec Beardsell[9], Georg Pirrung[10], Néstor Ramos-García[10], Wei Shi[11], Jie Fu[11], Rémi Corniglion[12], Anaïs Lovera[12], Josean Galván[13], Tor Anders Nygaard[14], Carlos Renan dos Santos[14], Philippe Gilbert[15], Pierre-Antoine Joulin[15], Frédéric Blondel[15], Eelco Frickel[16], Peng Chen[17], Zhiqiang Hu[17], Ronan Boisard[18], Kutay Yilmazlar[19], Alessandro Croce[19], Violette Harnois[20], Lijun Zhang[21], Ye Li[21], Ander Aristondo[22], Iñigo Mendikoa Alonso[22], Simone Mancini[23], Koen Boorsma[23], Feike Savenije[23], David Marten[24], Rodrigo Soto-Valle[24], Christian W. Schulz[25], Stefan Netzband[25], Alessandro Bianchini[26], Francesco Papi[26], Stefano Cioni[26], Pau Trubat[27], Daniel Alarcon[27], Climent Molins[27], Marion Cormier[28], Konstantin Brüker[28], Thorsten Lutz[28], Qing Xiao[29], Zhongsheng Deng[29], Florence Haudin[30], Akhilesh Goveas[31]

[1]National Wind Technology Center, National Renewable Energy Laboratory, Golden, CO 80401, USA
[2]Mechanical Engineering Department, Politecnico di Milano, Milano, 20156, Italy
[3]Laboratory of Fluid-Machines, Dipartimento di Energia, Politecnico di Milano, Milano, 20156, Italy
[4]Wind Department, Bureau Veritas, Paris, 92937, France
[5]Marine Division, Research Department, Bureau Veritas, Saint-Herblain, 44818, France
[6]Wind Turbine Technologies, Centro Nacional de Energías Renovables, Sarriguren, 31621, Spain
[7]Integrated Simulation Department, China General Certification Center, Beijing, 100013, China
[8]Research Institute, China State Shipbuilding Corporation, Chongqing, 401122, China
[9]Offshore Technology Department, DNV, Bristol, BS2 0PS, UK
[10]Department of Wind Energy, Technical University of Denmark, Lyngby, 2800, Denmark
[11]State Key Laboratory of Coastal and Offshore Engineering, Dalian University of Technology, Dalian, 116024, China
[12]Département Electrotechnique et Mécanique des Structures, Électricité de France, Paris, 91120, France
[13]Wind Energy Department, eureka!, Errigoiti, 48309, Spain
[14]Department of Wind Energy, Institute for Energy Technology, Kjeller, NO-2027, Norway
[15]Département Mécanique des Fluides~~Offshore Wind and Ocean Energies~~, I~~nstitut F~~rançais du P~~étrole~~ Energies ~~N~~nouvelles, ~~Paris~~Rueil-Malmaison, 92852, France
[16]Research and Development, Maritime Research Institute Netherlands, Wageningen, 6708, The Netherlands
[17]Marine, Offshore and Subsea Technology Group, Newcastle University, Newcastle, NE1 7RU, UK
[18]Aerodynamic Department, Office National d'Etudes et de Recherches Aérospatiales, Paris, 92190, France
[19]Deptartment of Aerospace Science and Technology, Politecnico di Milano, Milano, 20156, Italy
[20]Floating Offshore Group, PRINCIPIA, La Ciotat, 13600, France
[21]Wind Energy Group, Shanghai Jiao Tong University, Shanghai, 200240, China
[22]Department of Offshore Renewable Energy, Tecnalia Research & Innovation, Donostia-San Sebastián, 20009, Spain
[23]Wind Energy Department, Netherlands Organisation for Applied Scientific Research, Petten, 1755, The Netherlands
[24]Wind Energy Department, Technische Universität Berlin, Berlin, 10623, Germany
[25]Fluid Dynamics and Ship Theory, Hamburg University of Technology, Hamburg, 21073, Germany
[26]Department of Industrial Engineering, University of Florence, Florence, 50139, Italy

[27]Department of Civil and Environmental Engineering, Universitat Politècnica de Catalunya, Barcelona, 08034, Spain
[28]Wind Energy Research Group, University of Stuttgart, Stuttgart, 70569, Germany
[29]Department of Naval Architecture, Ocean and Marine Engineering, University of Strathclyde, Glasgow, G4 0LZ, UK
[30]Research and Development Department, Vulcain Engineering, Neuilly-sur-Seine, 92200, France
[31]Department of Load Engineering, WyndTek, Delft, 2628, The Netherlands

Correspondence to: Roger Bergua (roger.bergua@nrel.gov)

Abstract. This paper provides a summary of the work done within Phase III of the Offshore Code Comparison~~,~~ Collaboration, Continued, with Correlation and unCertainty (OC6) project ~~(OC6)~~, under International Energy Agency Wind Technology Collaboration Programme Task 30. This phase focused on validating the aerodynamic loading on a wind turbine rotor undergoing large motion caused by a floating support structure. Numerical models of the ~~Danish~~ Technical University of Denmark 10~~-~~ MW reference wind turbine were validated using measurement data from a 1:75 scale test performed during the UNsteady Aerodynamics for FLOating Wind (UNAFLOW) project and a follow-on experimental campaign, both performed at the Politecnico di Milano wind tunnel. Validation of the models was performed by comparing the loads for steady (fixed platform) and unsteady ~~wind conditions~~ (harmonic motion of the platform) wind conditions. For the unsteady wind conditions, the platform was forced to oscillate in the surge and pitch directions under several frequencies and amplitudes. These oscillations result in a wind variation that impacts the rotor loads (e.g., thrust and torque). For the conditions studied in these tests, the system aerodynamic response was almost steady~~ state aerodynamicsmainly described a quasi steady aerodynamic behavior~~. Only a small hysteresis in airfoil performance undergoing angle of attack variations in attached flow was observed. During the experiments, the rotor speed and blade pitch angle were held constant. However, in real wind turbine operating conditions, the surge and pitch variations would result in rotor speed variations and/or blade pitch actuations, depending on the wind turbine controller region that the system is operating. Additional simulations with these control parameters were conducted to verify the fidelity ~~between~~of different models. Participant results showed, in general, a good agreement with the experimental measurements and the need to account for dynamic inflow when there are changes in the flow conditions due to the rotor speed variations or blade pitch actuations in response to surge and pitch motion. Numerical models not accounting for dynamic inflow effects predicted rotor loads that were 9 % lower in amplitude during rotor speed variations and 18 % higher in amplitude during blade pitch actuations.

Formatted: Not Highlight

1 Introduction

The objective of Phase III of the Offshore Code Comparison Collaboration, Continued, with Correlation and unCertainty (OC6) project ~~is~~was to ~~validate~~evaluate the accuracy of aerodynamic load predictions by offshore wind modeling tools for a floating offshore wind turbine (FOWT). FOWT platforms can experience significant translational and rotational motions affecting the system dynamics and loads (Veers et al., 2022).

The OC6 project is part of an ongoing effort under ~~Wind Task 30 of the~~ International Energy Agency Wind Technology Collaboration Programme (IEA Wind) Task30 to verify and validate offshore wind turbine model~~l~~ling tools (IEA~~nternational~~

Energy Agency Wind Task 30, 2022). To validate the aerodynamic loading on the wind turbine under large motions, participants in OC6 Phase III modeled a 1:75 scaled version of the Danish Technical University of Denmark (DTU) 10- MW reference wind turbine (RWT) (Bak et al., 2013) examined in the UNAFLOW (Unsteady Aerodynamics for FLOating Wind (UNAFLOW) project (Fontanella et al., 2021a; and Fontanella et al., 2021b) and a follow-on experimental campaign. For such configuration, the group ran a series of simulations, including steady and unsteady wind conditions due to the platform motion, and compared the resulting rotor loads and wake behavior from the experiments and the different modeling tools. The rotor loads were also compared between different modeling approaches to assess the potential advantages and disadvantages of models of different fidelity. This paper summarizes the work done within the OC6 Phase III project.

The organization of the remainder of the paper is as follows.: Section 2 provides a definition of the scaled model and testing performed. Section 3 provides a description of the active participants involved in OC6 Phase III and their modeling approaches. Section 4 then summarizes the load cases that were performed for the verification and validation. Finally, Sections 5 and 6 provide some example results from the project and the conclusions drawn.

2 Model Definition

To validate the accuracy of the rotor loads for a FOWT, measurement data from two wind tunnel experimental campaigns were used. Both campaigns were conducted in the Politecnico di Milano wind tunnel (13.84 m wide xby 3.84 m high xby 35 m long) and used a 1:75 scaled version of the DTU 10- MW RWT. The blades were straight, without cone angle, and rigid. The blade properties can be found in Table 1. The aerodynamic center of the different radial stations is coincident with the blade pitch axis. Its position along the chord, as measured from the leading edge, is given in Table 1.

Table 1: Distributed blade properties

Radial Station	Distance along pitch axis from blade root [m]	Chord [m]	Aerodynamic twist [deg]	Aerodynamic center [% chord]	Relative thickness [%]
1	0.00000	0.05585	17.07668	50.00	100.00
2	0.05817	0.05678	17.04199	48.76	75.88
3	0.13641	0.07573	15.77593	35.76	17.91
4	0.21766	0.10620	12.30509	29.08	11.11
5	0.30059	0.11490	9.98299	29.00	9.97
6	0.38379	0.11044	8.65143	29.00	9.97
7	0.46581	0.10236	7.56522	29.00	9.97
8	0.54530	0.09272	6.38165	29.00	9.97
9	0.62105	0.08288	5.08008	29.00	9.97
10	0.69211	0.07356	3.79042	29.00	9.97
11	0.75778	0.06516	2.61685	29.00	9.97

12	0.81765	0.05778	1.59090	29.00	9.97
13	0.87153	0.05141	0.71754	29.00	9.97
14	0.91947	0.04604	0.03751	29.00	9.97
15	0.96171	0.04163	-0.53510	29.00	9.97
16	0.99860	0.03796	-1.03393	29.00	9.97
17	1.03056	0.03440	-1.46251	29.00	9.97
18	1.05807	0.03054	-1.61172	29.00	9.97
19	1.08162	0.02541	-1.60710	29.00	9.97
20	1.10166	0.00998	-1.72236	29.00	9.97

Two-dimensional sectional-model experiments were conducted in the DTU Red wind tunnel to characterize the airfoil polars ~~in~~with smooth and ~~turbulent flows~~rough surface conditions (Fontanella et al., 2021b). The airfoil polars with the lift and drag coefficients for the different angles of attack at the 20 radial stations shown in Table 1 for ~~turbulent flow~~ rough surface conditions were provided to the participants. Each airfoil polar contains seven sets of lift and drag coefficients for Reynolds numbers ranging between 5E4 and 2E5 (Robertson et al., 2022).

The rest of the model geometry ~~of the model~~ (e.g., tower, rotor overhang) was dependent on the testing campaign being studied. The first data set was developed during the UNAFLOW project (Fontanella et al., 2021a). The testing was similar to ~~the one~~that performed during the LIFES50+ project (Bayati et al., 2017). However, for the UNAFLOW test the tower was considered rigid and included a negative tilt angle of 5 deg to offset the wind turbine tilt angle~~:~~, resulting in a rotor perpendicular to the wind tunnel floor. The second data set is from a follow-on testing campaign performed during 2021 in the same wind tunnel. It used the same rotor but a different nacelle and tower length (also rigid) than the one used in the UNAFLOW project.

Figure 1 shows the scaled DTU 10~~-~~ MW RWT during the two testing campaigns. For simplicity, the UNAFLOW campaign is described as e~~E~~xperiment 1 and the follow-on campaign is described as e~~E~~xperiment 2. An air density of 1.177 kg/m~~^3~~^{3} is considered for both campaigns.

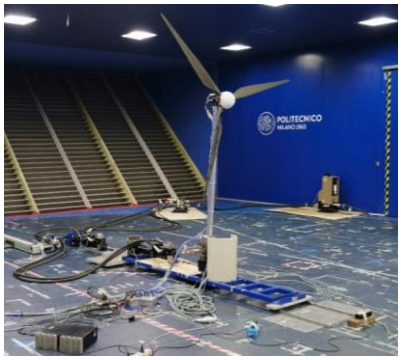

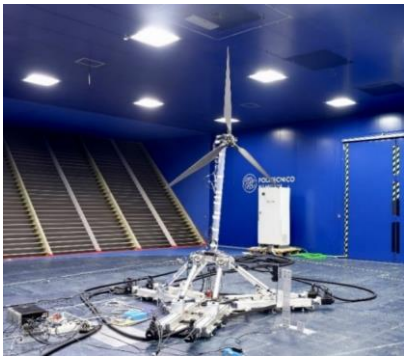

Figure 1: The 1:75 scaled DTU 10- MW ~~RWT~~ reference wind turbine in the Politecnico di Milano wind tunnel. Left: Testing during the UNAFLOW campaign (eExperiment 1). Right: Testing during the follow-on campaign (eExperiment 2).

Figure 2 shows a schematic representation of the wind turbine tested in both campaigns and the two coordinate systems used in this project. Table 2 provides the geometrical properties for these two campaigns.

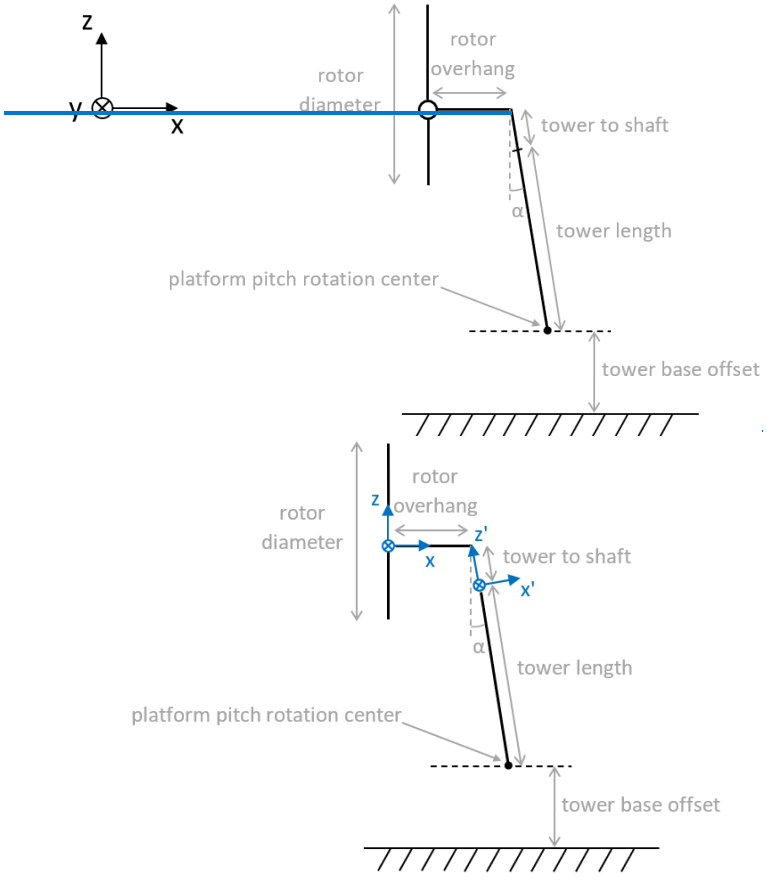

Figure 2: Schematic representation of the wind turbine system and the coordinate systems (hub fix and tower top).

Table 2: System geometry

Parameter	UNAFLOW (eExperiment 1)	Follow-on campaign (eExperiment 2)	DTU 10 MW RWT (full scale)
Rotor diameter (Ø)	2.38132 m		178.3
Blade length	1.10166 m		86.37
Hub diameter	0.178 m		5.6 m
Rotor overhang	0.09467 m	0.139 m	7.1 m
Tilt angle (α)	5 deg		5 deg
Tower to shaft distance	0.03667 m	0.064 m	2.75 m
Tower length	1.6057 m	1.400 m	115.63 m
Tower base offset	0.450 m	0.730 m	-

Formatted Table
Formatted: Font: (Default) Arial
Formatted: NREL_Table_Content

The eExperiment 1 includes steady and unsteady wind conditions. The unsteady wind conditions were induced by means of forced harmonic oscillations in the surge direction (i.e., fore-aft translation). The forced motion was achieved through two hydraulic actuators at the tower base. This campaign includes load measurements with a 6 degree-of-freedom (DOF) load cell at the tower top location, 6- DOF load cell at the tower base, hot-wire probes to measure the wind speed along and across the wake, and particle image velocimetry (PIV) to study the blade tip vortex behavior.

The eExperiment 2 used a 6- DOF robot at the base instead of the two hydraulic actuators used for the fore-aft translation in the eExperiment 1. During this testing, some of the conditions studied during the eExperiment 1 were tested again. In addition, for the unsteady wind cases, equivalent tests in terms of rotor apparent wind were tested, but using platform pitch motion instead of surge motion. Equivalent measurements for tower top loads were recorded during this test campaign, but information about the wind turbine wake was not recorded (i.e., hot-wire and PIV measurements are not available).

During eExperiment 1, the rotor was kept rotating at a constant speed. However, eExperiment 2 used a different rotor speed controller, resulting in some rotor speed oscillations. These rotor speed variations can impact the amplitude and phase of the rotor loads, which could have important implications for the torque due to the rotor inertia. Politecnico di Milano tried to remove these rotor speed variations by means of an analytical postprocessing.

The hub height in both experiments is also slightly different. The relatively small distance (close to 0.5 m, or 0.2 rotor diameter) between the blade tip and the wind tunnel ceiling might affect the wake expansion in the vertical direction, and thus the induction in the rotor area.

During the testing campaigns, the wind turbulence intensity in the region covered by the rotor was close to 2 % (Bayati et al., 2018). Moreover, the wind speed was fairly constant over the rotor- swept area (Bayati et al., 2018). For the numerical models, it was decided to use a spatially uniform steady inflow.

Finally, Politecnico di Milano performed a postprocessing of the load measurements to remove the inertial loads (Mancini, 2020). The loads studied in this paper are purely aerodynamic. Participants modeled a rigid tower, and a rigid rotor, and extracted the rotor aerodynamic loads.

3 Participants and Modeling Approach

A total of 29 academic and industrial partners from 10 different countries ~~actively~~ participated in OC6 Phase III. Those actively involved were~~:~~ Bureau Veritas (BVMO, France), Centro Nacional de Energías Renovables (CENER, Spain), China General Certification Center (CGC, China), China State Shipbuilding Corporation (CSSC, China), Det Norsk Veritas (DNV, United Kingdom), Technical University of Denmark (DTU, Denmark), Dalian University of Technology (DUT, China), Électricité de France (EDF, France), eureka! (EURE, Spain), Institute for Energy Technology (IFE, Norway), ~~Institut Français du Pétrole Energies Nouvelles~~IFP Energies nouvelles (IFPEN, France), Maritime Research Institute Netherlands (MAR, The Netherlands), National Renewable Energy Laboratory (NREL, USA), Newcastle University (NU, United Kingdom), Office National d'Etudes et de Recherches Aérospatiales (ON, France), Politecnico di Milano – POLI-Wind Laboratory (POLI-W, Italy), Politecnico di Milano (POLIMI, Italy), PRINCIPIA (PRI, France), Shanghai Jiao Tong University (SJTU, China), Tecnalia (TECN, Spain), Netherlands Organization for Applied Scientific Research (TNO, The Netherlands), Technische Universität Berlin (TUB, Germany), Hamburg University of Technology (TUHH, Germany), Università degli Studi di Firenze (UNIFI, Italy), Universitat Politècnica de Catalunya (UPC, Spain), University of Stuttgart (USTUTT, Germany), University of Strathclyde (UoS, United Kingdom), Vulcain Engineering (VULC, France), and WyndTek (WTEK, The Netherlands).

The participants used modeling approaches of different fidelity to study the system: blade element momentum (BEM) theory, dynamic BEM (DBEM) that accounts for dynamic inflow ~~model~~effect, generalized dynamic wake (GDW), free-vortex wake (FVW), and blade-resolved or actuator-line ~~-~~based computational fluid dynamics (CFD).

The BEM, DBEM, GDW, some FVW ~~(e.g., lifting line and lifting surface)~~ and the actuator-line-based CFD approaches are based on the lifting line theory. In these approaches, the airfoil polar data is used as an input for the model. The airfoil polar provides information about the lift and drag coefficients as a function of the angle of attack. Participants can use the airfoil polar information as a look-up table (static polars approach) or account for unsteady airfoil aerodynamics. The unsteady airfoil aerodynamics accounts for the flow hysteresis in the lift and drag coefficients under unsteady wind and wind turbine operating conditions (e.g., blade pitch actuations). The flow hysteresis can occur during attached flow (e.g., linear region in the airfoil polar) or flow separation, including dynamic stall (e.g., nonlinear region in the airfoil polar). These unsteady effects are computed by the modeling tools and depend on the underlying theory considered. The lifting surface and 3D panel FVW ~~3D panel method and~~as well as ~~-~~the blade-resolved CFD do not use the airfoil polar data as input. Instead, they use a surface mesh based on the blade geometry. One computer aided design (CAD) file of the blade was provided to the participants. In this case, it may be challenging to reproduce the airfoil polars behavior due to the relatively small Reynolds numbers during the experiment (mainly below 1E5). Small Reynolds numbers may increase the boundary layer thickness, resulting in larger drag and smaller lift coefficients.

Sectional aerodynamic loads are computed on the basis of the local inflow velocity.~~The aerodynamic rotor loads are computed according to the inflow velocity.~~ The local inflow velocity is the sum of the relative velocity (e.g., due to the incoming wind, the rotor rotation, and the platform motion) and the induced velocity (i.e., the velocity change due to the interaction with the

rotor). The steady BEM theory assumes that the wake reacts instantaneously. In this equilibrium wake assumption, the induced velocities (based on the axial and tangential induction factors) are quasi-steady. However, in reality, it takes time (delay) for the wake to respond to a change in the flow conditions. This change in the flow conditions can be due to changes in the incoming wind or the turbine response (e.g., rotor speed variations, blade pitch variations, and platform motions). The BEM theory with dynamic inflow model (also referred to as dynamic wake) tries to capture the unsteady aerodynamic response ~~due to~~from this delayed wake response by means of a correction consisting of low-pass filters over the quasi-steady induced velocities. In GDW, dynamic inflow is explicitly calculated by representing the induced velocity in terms of series expansion of radial and azimuthal basis functions within a governing equation that takes into account ~~through the use of~~ an apparent mass ~~in the induction calculation~~. Dynamic inflow is intrinsically captured by FVW because induction is calculated directly from the time-dependent trailing and shed vorticity and by CFD because of the explicit solving of the momentum and continuity equations.

A list of the participants is provided in Table 3, which also shows the modeling approaches adopted and the codes used. Some participants decided to use more than one modeling approach, and some used different codes. A total of 54 numerical models were involved in this validation.

Table 3: Summary of participants, codes, and modeling approach used

Participant	Code	Wake/Induction Model					Airfoil Model		
		BEM	DBEM	GDW	FVW	CFD	Static	Unsteady	Resolved
BVMO	Opera	X	X				X		
CENER	AeroVIEW				X			X	
	OpenFOAM					X			X
CGC	Bladed		X					X	
CSSC	Q~~b~~Blade				X			X	
DNV	Bladed		X					X	
DTU1	HAWC2		X					X	
	HAWC2-MIRAS				X	X		X	
DTU2	HAWC2		X[a]					X	
DUT	OpenFAST		X					X	
EDF1	DIEGO	X	X				X		
EDF2	DIEGO	X	X		X			X	
EURE1	OpenFAST	X	X				X		
EURE2	OpenFAST	X	X		X			X	
IFE	3Dfloat		X				X		
	RotorVex			X				X	
IFPEN	Aerodeep		X					X	

Participant	Code	Wake/Induction Model					Airfoil Model		
		BEM	DBEM	GDW	FVW	CFD	Static	Unsteady	Resolved
	Castor				X			X	
MAR	aNySIM-XMF	X					X		
NREL1	OpenFAST	X	X				X		
NREL2	OpenFAST	X	X		X			X	
NU	DARWind	X					X		
ON	PUMA				X		X		
POLI-W	Cp-Lambda	X		X			X		
POLIMI	OpenFOAM^					X	X		
PRI	DeepLines Wind		X					X	
SJTU	STAR-CCM+					X			X
TECN	OpenFAST	X	X					X	
TNO	AeroModule		X		X			X	
TUB	Q~~b~~Blade				X			X	
TUHH	*pan*MARE				X		X		
UNIFI	OpenFAST CONVERGE		X			X	X	X	
UPC	FloaWDyn OpenFAST	X			X		X	X	
USTUTT	FLOWer					X			X
UoS	OpenFOAM					X			X
VULC	OpenFAST	X	X				X		
WTEK	Ashes		X					X	
Number of numerical models		13	20	2	12	7			

[a]Near-wake model.
^OpenFOAM modified version.

~~FVW models can model the blades by means of different theories (e.g., lifting line, lifting surface, and 3D panel method). However, all FVW models used by participants in this project are based on the lifting line theory.~~

EDF, EURE, and NREL used two different model~~l~~ing approaches based on the lifting line theory within the same code ~~(denoted with "1" and "2"). where~~ The models denoted with "1" use a static polars approach while the models denoted with "2" account for unsteady airfoil aerodynamics.~~the difference between them is only in terms of the airfoil data. For these participants, the models denoted with "1" account for the lift and drag coefficients from the airfoil polar as a look-up table (static polars approach) while the models denoted with "2" account for unsteady airfoil aerodynamics. The unsteady airfoil aerodynamics~~

~~accounts for the flow hysteresis in the lift and drag coefficients under unsteady wind and wind turbine operating conditions (e.g., blade pitch actuations). The flow hysteresis can occur during attached flow (e.g., linear region in the airfoil polar) or flow separation, including dynamic stall (e.g., nonlinear region in the airfoil polar). These unsteady effects are computed by the modeling tools and depend on the underlying theory considered. The inclusion of numerical models with different fidelity allows identification of the differences between them.~~

Other ~~For the rest of the models, the ones u~~participants using a lifting line approach with static polars were~~:~~: BVMO, IFE (DBEM), MAR, NU, ON, POLI-W, POLIMI, TUHH, UNIFI (FVW), UPC (BEM), and VULC. ~~P~~Other participants using a lifting line approach with unsteady airfoil aerodynamics were: CENER (FVW), CGC, CSSC, DNV, DTU1 ~~(DBEM and FVW)~~, DTU2, DUT, IFE (GDW), IFPEN, PRI, TECN, TNO, TUB, UNIFI (DBEM), UPC (FVW), and WTEK.

All FVW models used by participants are based on the lifting line theory. For the CFD models, ~~T~~three participants used an actuator-line ~~-~~based ~~CFD~~ approach~~:~~ (DTU1, POLIMI, and UNIFI) and ~~. In the actuator-line model, the blades are discretized as rotating lines of actuator points and the aerodynamic forces are computed using static polars (POLIMI, UNIFI) or unsteady airfoil aerodynamics (DTU1). F~~four ~~CFD p~~participants used a blade-resolved approach~~:~~ (CENER, SJTU, USTUTT, and UoS). ~~The blade-resolved approach uses a surface mesh based on the blade geometry. One computer aided design (CAD) file of the blade was provided to the participants. For this approach, it may be challenging to reproduce the airfoil polars behavior due to the relatively small Reynolds numbers during the experiment (mainly below 1E5). Small Reynolds numbers may increase the boundary layer thickness, resulting in larger drag and smaller lift coefficients.~~ ~~FVW models can model the blades by means of different theories (e.g., lifting line, lifting surface, and 3D panel method). However, all FVW models used by participants in this project are based on the lifting line theory.~~

4 Load Cases

A stepwise validation procedure was performed in the OC6 Phase III project taking advantage of the two experimental campaigns carried out in the Politecnico di Milano wind tunnel.

Table 4 provides a summary of the simulations that are presented in Section 5, including one steady wind condition (L~~l~~oad C~~c~~ase 1.1) and unsteady wind conditions under platform surge (L~~l~~oad C~~c~~ases 2.X) and platform pitch motion (L~~l~~oad C~~c~~ases 3.X). For the pitch motion, the equivalent longitudinal amplitude can be approximated by multiplying the sine of the platform pitch angle by the distance from the hub to the tower base. Load C~~c~~ases 3.5 and 3.7 result~~s~~ in the same rotor apparent wind (horizontal component) as L~~l~~oad C~~c~~ases 2.5 and 2.7, respectively. The rotor apparent wind in L~~l~~oad C~~c~~ase 3.1 is slightly lower than in load case 2.1 due to a limitation in the 6 ~~-~~DOF robot motion range.

Three additional load cases (2.12, 2.16, and 2.17) were included to examine conditions that might create more impactful unsteady aerodynamic responses due to changes in the flow conditions. There ~~is~~are no experimental data available for these conditions; thus, ~~and~~ they are ~~thus~~ used as verification cases only. Load C~~c~~ase 2.12 includes a platform surge oscillation at the

same frequency as Lload Cease 2.7, but with an amplitude that is one order of magnitude higher. Finally, Lload Ceases 2.16 and 2.17 are based on Lload Cease 2.12 but include some rotor speed and blade pitch variations.

Some numbers are skipped in the load case numbering sequence because there were more load cases that did not provide additional insight and are left out of the results of Section 5.

Table 4: Offshore Code Comparison Collaboration, Continued, with Correlation and unCertainty (OC6) Phase III load case simulations (summary)

Wind Conditions	Load Case	Wind Speed (U_0) [m/s]	Platform Motion			Rotor speed (Ω) [rpm]	Blade pitch angle (β) [deg]
			Direction	Frequency (f) [Hz]	Amplitude (A) [m] or [deg]		
Steady Wind	1.1	4.19	None			240	0
Unsteady Wind	2.1		Surge	0.125	0.125		
	2.5			1.0	0.035		
	2.7			2.0	0.008		
	2.12			2.0	0.080		
	2.16					240 ± 36	
	2.17					240	1.5 ± 1.5
	3.1		Pitch	0.125	3.000		0
	3.5			1.0	1.400		
	3.7			2.0	0.300		

The studied wind speed of 4.19 m/s and rotor speed of 240 rpm, in these load cases, is representative of the near rated condition for the DTU 10- MW RWT at model scale (tip speed ratio of 7.1). This wind speed was already corrected to account for the wind tunnel blockage (Robertson et al., 2022). The presence of the scaled wind turbine in the test section reduces the flow area compared to an unrestricted freestream. This flow area reduction results in an increased wind velocity in the rotor disk area. The blockage ratio between the rotor disk area and the wind tunnel cross- area was close to 8 % during the experiments. This corrected value of 4.19 m/s was used by participants using BEM, DBEM, GDW, and FVW approaches. Most participants using the CFD approach (POLIMI, UNIFI, USTUTT, and ~~UoS) included~~UoS) included the wind tunnel walls, ceiling, and floor in their numerical models, reproducing the confined system conditions. These boundary conditions were introduced in the CFD models by means of slip walls. A wind speed of 4 m/s was used by these participants.

In the study of unsteady aerodynamics, it is common to use reduced frequencies (Ferreira et al., 2022; ~~and~~ Mancini et al., 2020). The reduced frequency is a dimensionless number with higher values indicating a greater degree of unsteadiness. The reduced frequency (k) is related to the motion frequency (f), the rotor diameter ($Ø$), and the freestream wind (U_0) as stated in Eq. (1). The platform motion frequencies shown in Table 4 result in reduced frequencies of 0.071, 0.568, and 1.137.

$$k = f \cdot \frac{Ø}{U_0} \quad (1)$$

Formatted: Font: Italic
Formatted: Font: Italic
Formatted: Font: Italic
Formatted: Font: Italic
Formatted: Font: Italic
Formatted: Font: Italic

The platform motion amplitudes shown in Table 4 correspond to oscillations ranging from 0.6 to 9.375 m at full- scale (i.e., from 0.003 to 0.05 rotor diameter). In terms of periods at full -scale, the tests cover the range from 12.5 to 200 seconds (Mancini et al., 2020). Most FOWT testing is done with Froude-scaled models. However, in the two testing campaigns considered in this study, the scaling was based on the reduced frequency to try to preserve the relationship between the wind and the platform velocity. In this case, the wind velocity was scaled by a factor of 3 and the physical dimensions by 75 (Mancini et al., 2020). These amplitudes and periods are considered representative of different FOWT support structures.

The loads measured at the tower top during the experiments were oriented according to the tilted tower (Robertson et al., 2022x'-y'-z' coordinate system in Figure 2). These loads were first rotated according to the tilt angle and then translated to the hub location (x-y-z coordinate system in Figure 2) to make the comparison between the numerical models and the experiments easier.

During the processing of the experimental data, a significant 1P response corresponding to the blade passing frequency was observed. This frequency was due to a rotor asymmetry. The three blades were measuredweighted and one of the blades had a significant mass imbalance (~10 %). Moreover, a 2P was also present in the response. This could denoteimply an aerodynamic imbalance (e.g., one blade pitch error or blades with different aerodynamic performance). This aerodynamic imbalance would result in loads with a different mean value, as well as the presence of a 1P in the response, and the corresponding harmonics (e.g., 2P). To avoid the dynamic influence of this rotor asymmetry, the data from the experiments wasere low-pass filtered at 3 Hz. This cut-off frequency was a compromise to include the fastest platform motion in the experiments (2 Hz in Lload Ceases 2.7 and 3.7) and exclude the rotor asymmetry (1P frequency is 4 Hz for a rotational speed of 240 rpm). Thise low-pass filter also removes the tower shadow effect (e.g., the 3P excitation and the corresponding harmonics). Accordingly, participants did not include the tower influence in the wind in their numerical models or filtered it out in case it was included.

5 Results

In this section, a comprehensive overview of the studied load cases shown in Table 4 is presented and explained.

5.1 Steady Wind: Load Case 1.1

5.1.1 Aerodynamic Rotor Loads

Load Cease 1.1 focuses on ensuring that the aerodynamic models were implemented correctly by examining the aerodynamic rotor loads. Because Tthe rotor is perpendicular to the tunnel floor (i.e., there is no effective tilt angle), spatially uniform wind is considered, and the tower influence over the wind is not considered. Therefore, the resultant rotor loads are only *Fx* (thrust force) and *Mx* (torque).

Figure 3 shows the aerodynamic rotor thrust for Lload Cease 1.1. Figure 3 includes the results from the participants grouped according to the modeling approach from lower to higher fidelity (BEM < DBEM ≈ GDW < FVW < CFD). The results from

Formatted: Font: Italic

Formatted: Font: Italic

the two experimental campaigns are also included. There is a difference in the aerodynamic thrust between the two experiments (7 %). Experiment 1 shows less variation of the mean aerodynamic forces during the testing, indicating more reliable measurements. This difference in ~~the~~ Eexperiment 2 could be due to the influence of the cable bundle used for the sensors and power that is located behind the wind turbine (see Fig~~ure~~. 1) or a small blade pitch angle offset.

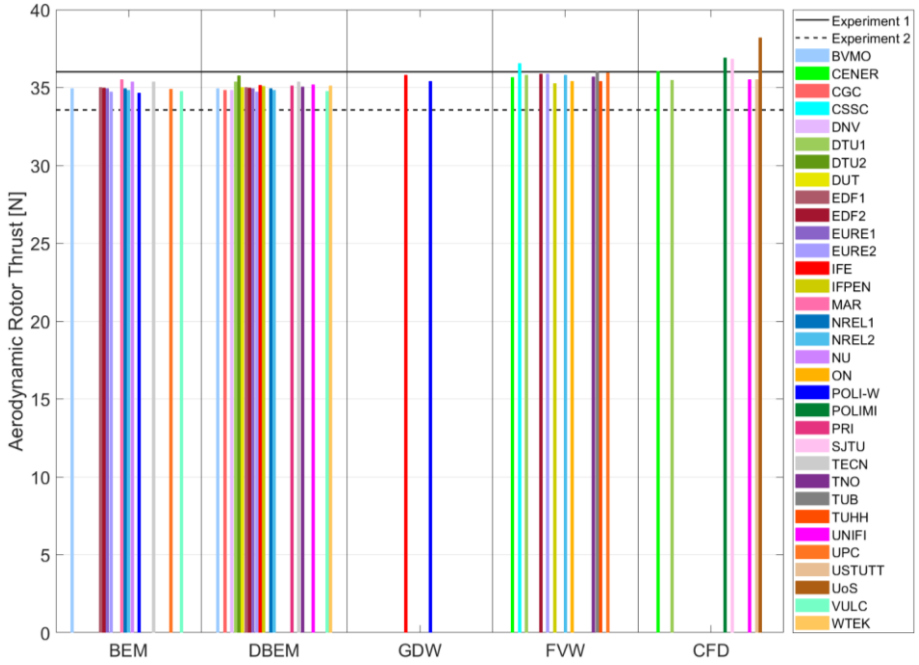

Figure 3: Aerodynamic rotor thrust in steady wind conditions (L~~l~~oad C~~c~~ase 1.1).

As Fig.~~ure~~ 3 shows, most numerical models predict an aerodynamic thrust force that is within the values observed in the experiments. Only some FVW and CFD solutions are slightly above the values observed in ~~the~~ Eexperiment 1. FVW solutions (based on the lifting line theory) return higher thrust values than BEM and DBEM solutions despite using the same airfoil polar data. When looking at the local inflow velocity along the blade (not shown), it can be noticed that the FVW models have slightly higher values. Since the rotational speed is fixed and the incoming wind is the same, this indicates that the FVW models have slightly different induction factors. By looking at the axial and tangential induction (not shown), FVW models have lower axial and higher tangential induction factors with both contributions adding to a higher local inflow velocity. Moreover, the lower axial induction factor in the FVW results in a higher angle of attack. Both, the higher local inflow velocity and the higher angle of attack, result in higher loads.

Formatted: Font color: Auto

Formatted: Font color: Auto

Formatted: Font color: Auto

Figure 4 shows the corresponding aerodynamic rotor torque for Lload Ccase 1.1. There is good agreement between both experiments while most numerical models underpredict the aerodynamic torque.

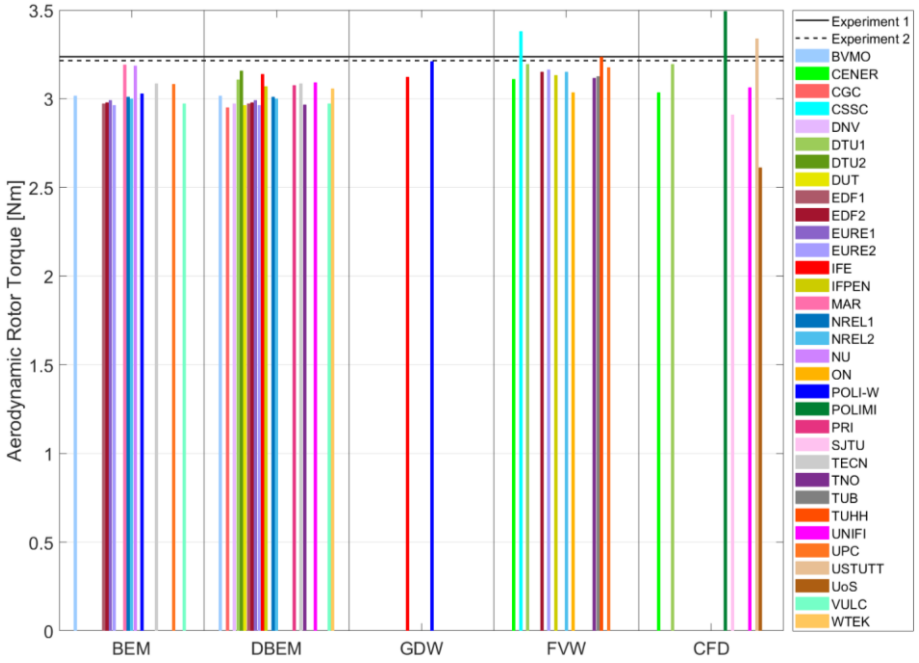

Figure 4: Aerodynamic rotor torque in steady wind conditions (Lload Ccase 1.1).

For steady wind conditions, no differences between BEM and DBEM are expected because there are no variations in terms of wind, rotor speed, or blade pitch angle. This expected behavior is observed within the participants using the same code with BEM and DBEM (i.e., BVMO, EDF, EURE, NREL, TECN, and VULC). Moreover, no differences between static polars and unsteady airfoil aerodynamics are expected because the angle of attack at each blade radial station is constant, and the rotor is planar (Li et al., 2022).

Most BEM and DBEM numerical models account for aerodynamic corrections commonly used in the design of wind turbines (e.g., hubblade root and blade tip losses). The lack of these corrections results in loads that are higher than expected.

Figure 5 ispresents a summary of the aerodynamic rotor thrust and torque based on modeling approach. The data from Fig.ure 3 and Fig.ure 4 haves been sorted from lower to higher within each modeling approach and then divided into four parts (quarters). The dots shown are indicative of the median (i.e., second quartile). The median and the quartiles provide information about both the center and the spread of the data. For example, the band around the median contains 50 % of the participants

results for a given modeling approach. The upper and lower ranges, respectively, contain the remaining 25 % of the participant results, respectively. This statistical information can be considered equivalent to thate one obtained from a box plot. Using the median instead of the mean avoids the potential impact of outliers in the data. The subindex next to each modeling approach indicates the number of results available from the participants. For the GDW approach there areis only data from two participants. In this case, the median is equivalent to the mean and the range is determined by the maximum and minimum value.

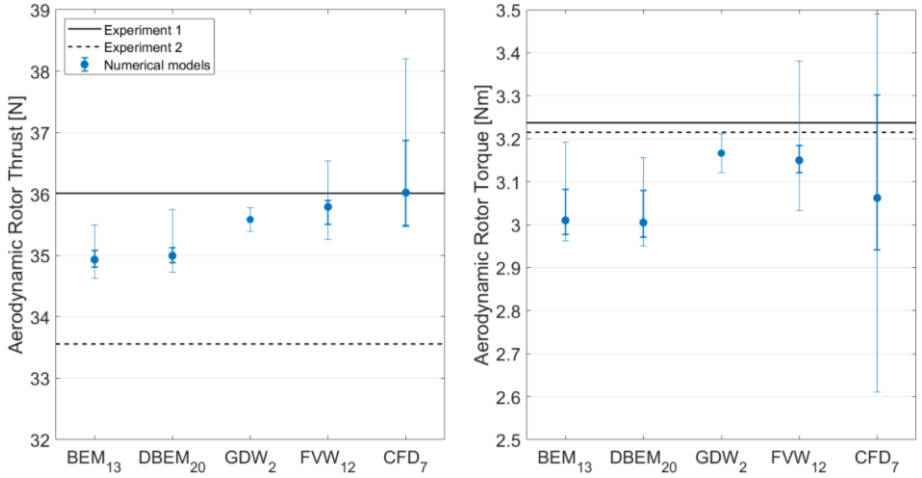

Figure 5: Aerodynamic rotor thrust (left) and torque (right) during the steady wind condition. Median and quartiles for the different simulation approaches.

5.1.2 Hot-Wwire Measurements

For the Eexperiment 1, hot-wire measurements were taken during the steady wind condition. A hot-wire anemometer probe traversed the along-wind direction (*x*-direction in Fig.ure 2) and the cross-wind direction (*y*-direction in Fig.ure 2). Participants using FVW or CFD can get insights about the wind turbine wake behavior. For reference, Fig.ure 6 includes the wake behavior for NREL (FVW) as well as the hot-wire locations (black dots) and PIV plane (graey rectangle).

Formatted: Font: Italic

Formatted: Font: Italic

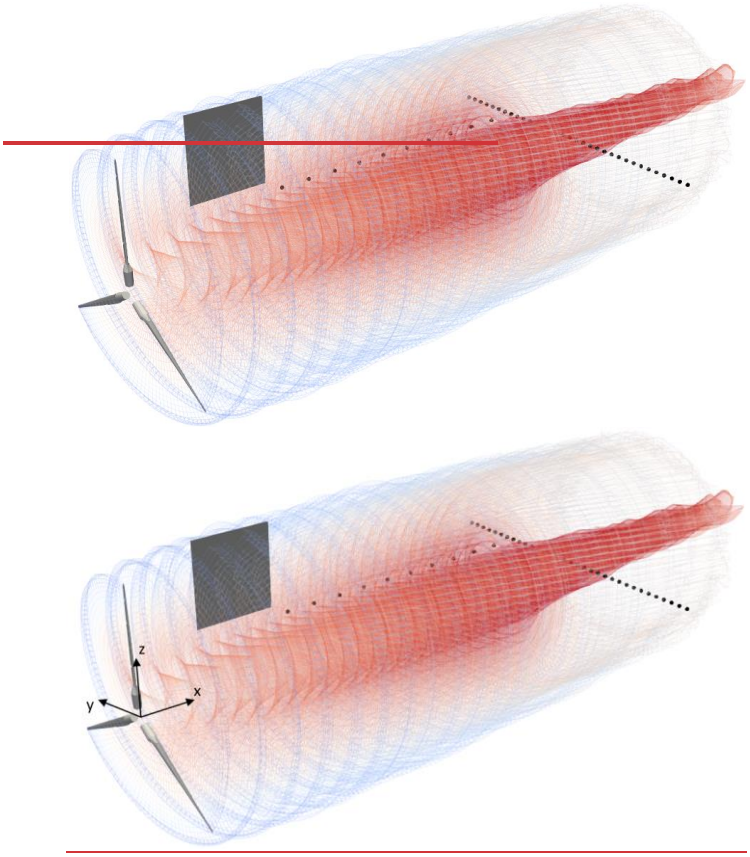

Figure 6: Wind turbine wake behavior in OpenFAST (fFree-vVortex wWake approach) during steady wind conditions.

For the along-wind measurements, the hot-wire anemometer probe started with a 0.9 m offset in the *y*-direction and moved between 2.18 and 5.48 m along the *x*-direction from the hub location (i.e., 0.9 and 2.3 rotor diameters (Ø) downwind). Eleven points every 0.33 m along the *x*-direction were measured. Figure 7 (left) shows the corresponding longitudinal wind speed (*u*) measured by the hot-wire probe and the output from the FVW and CFD participants. The wind speed in the figure corresponds to the average value at the location of interest during one rotor revolution. The ~~FVW solutions are denoted with a dashed line while the~~ CFD ~~ones~~solutions are denoted with a solid line while the FVW solutions (12 outputs) are denoted by a gray area due to some limitations. For example, the wind speed obtained within the wake ~~FVW response~~ is a function ~~determined by~~of

Formatted: Font: Italic

Formatted: Font: Italic

Formatted: Font: Italic

the wake length chosen by the FVW participants. Moreover, the lack of viscous diffusion in the FVW models makes the characterization of the wake recovery~~characterization~~ challenging in the absence of meandering from turbulence. Despite these limitations, ~~it~~we would ~~be~~ expect~~ed~~ a decent agreement between FVW approaches in the near wake ~~-~~because~~,~~. ~~I~~in this region the viscous diffusion should not be driving the wake response. However, a significant spread of results was observed for FVW participants. Figure ~~8~~7 (right) shows the inflection wake recovery point for the experiment and the CFD participants. This is the point where the wake velocity shows a minimum and from that point starts to recover. The outputs from individual FVW participants are not included ~~due to the lack of viscous diffusion~~for the reasons explained previously. ~~For these participants the inflection wake recovery point cannot be predicted accurately and, in some cases, the wake recovery may never occur.~~ It is also worth noting that the ambient turbulence observed in the wind tunnel should result in a shorter inflection wake recovery point. The ambient turbulence intensity during the testing was close to 2 % while participants considered a steady wind condition. The maximum wake velocity deficit observed in the experiment is around u/U_0 = 0.44. Most numerical models show a wind speed deficit like in the experiment. However, there are some differences regarding the inflection wake recovery point. For ~~some~~most CFD participants, the inflection wake recovery point occurs at a distance equal to or after 5.48 m (i.e., 2.3 diameters downwind). ~~The inflection wake recovery point can be impacted by the simulation settings used by the different participants. For example, for FVW approaches, the inflection point will artificially depend on the wake length chosen. FVW participants modeling a longer wake may never see the wake recover in the window length studied. Moreover, the wake recovery may not happen as viscous diffusion is often not included in the FVW models.~~

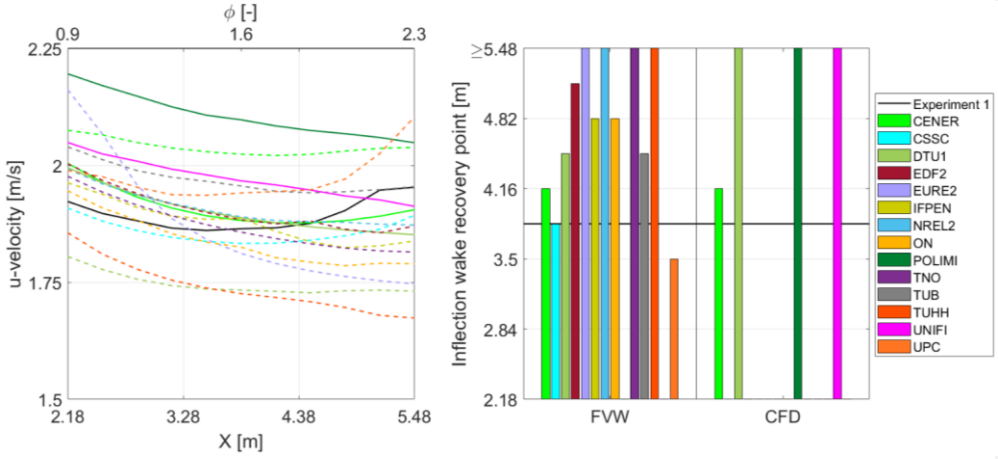

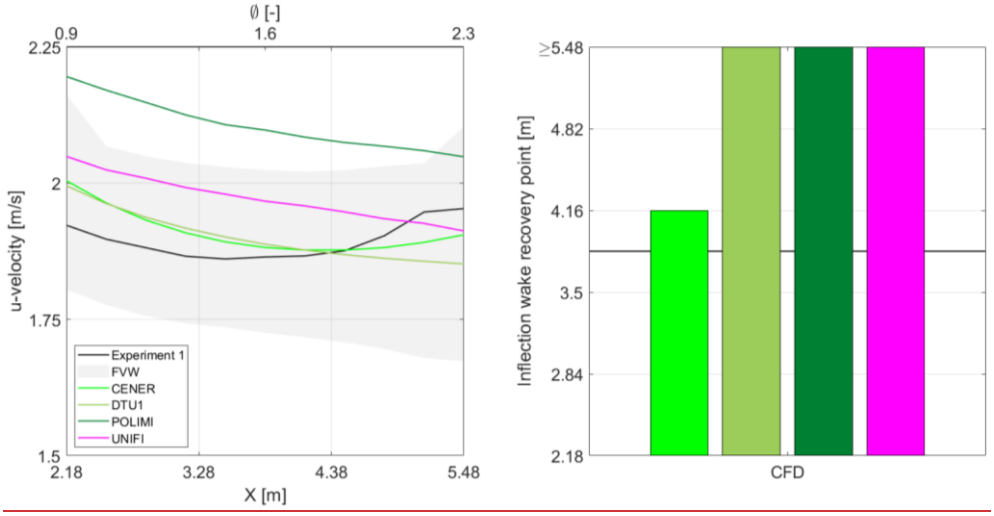

Figure 7: Left: Averaged hot-wire longitudinal velocity for one rotor revolution in the along-wind direction (*y* = 0.9 m, *z* = hub height) during steady wind conditions. Right: Inflection wake recovery point location.

As Fig. ~~ure~~ 7 shows, the last hot-wire measurement at the point 5.48 m downwind seems to be off. This results in a lower-than-expected wake slope at the end of the window studied ~~lower than expected~~. This unexpected behavior is not observed in other tests and measurements (see next section: analysis of the hot-wire cross-wind data).

For the cross-wind measurements, the hot-wire started at the hub location, but 5.48 m downwind and moved from -1.60 m to 1.60 m in the *y*-direction with a spatial discretization of 0.10 m (33 points). However, for this specific steady wind condition the hot-wire probes during the experiment were shifted 0.13 m in the *y*-direction, effectively measuring from -1.47 m to 1.73 m. This introduces a small difference in the spatial discretization between the numerical models and the experiment. Figure 8 (left) shows the longitudinal wind speed measured by the hot-wire probe and the output from the participants. The wind speed in Fig. ~~ure~~ 8 corresponds to the average value during one rotor revolution and the pattern used for the FVW and CFD participants is the same as the one in Fig. ~~ure~~ 7. Figure 8 also includes ~~one~~a rectangular gre~~a~~y area that denotes the region covered by the wind turbine rotor. Moreover, one vertical dotted line denotes the corresponding location of the last hot-wire ~~(HW)~~ along-wind ~~(AW)~~ measurement point ("Last HW AW point"). This point in the space (*x* = 5.48 m, *y* = 0.9 m, *z* = hub height) is measured by both the along-wind and the cross-wind hot-wires. Interestingly, the longitudinal velocity measured by the cross-wind hot-wire is above 2 m/s. This measured value is aligned with the expected behavior. The different value reported by the along-wind and cross-wind hot-wires indicates that there is some uncertainty in the measurement.

As ~~it~~ can be observed from Fig. ~~ure~~ 8 (left), in the experiment the longitudinal wind velocity drops to a value between 1.75 and 2.75 m/s in the region covered by the wind turbine rotor. The velocity deficit profile mainly depends on the thrust coefficie nt

Formatted: Font: Italic
Formatted: Font: Italic
Formatted: Font: Italic
Formatted: Font: Italic
Formatted: Font: Italic
Formatted: Font: Italic
Formatted: Font: Italic

along the blade span. For the numerical models, minimaums in the velocity field occur between 0.5 and 1.1 m from the hub center (y = 0 m), where the thrust coefficient tends to be at a maximum. For the experiment, the minimaums in the velocity deficit are similar but only occur around 0.8 m from the hub center. Moreover, most numerical models return a wind speed slightly above the freestream wind (i.e., 4.19 m/s) behind the hub location (x = 5.48 m, y = 0 m, z = hub height), while the experiment shows a significant velocity deficit. The reason is that most numerical models do not include the hub nose blockage (see Fig. ure 1 [left]). Only some CFD participants (e.g., UNIFI and CENER) included the hub nose and nacelle geometry.

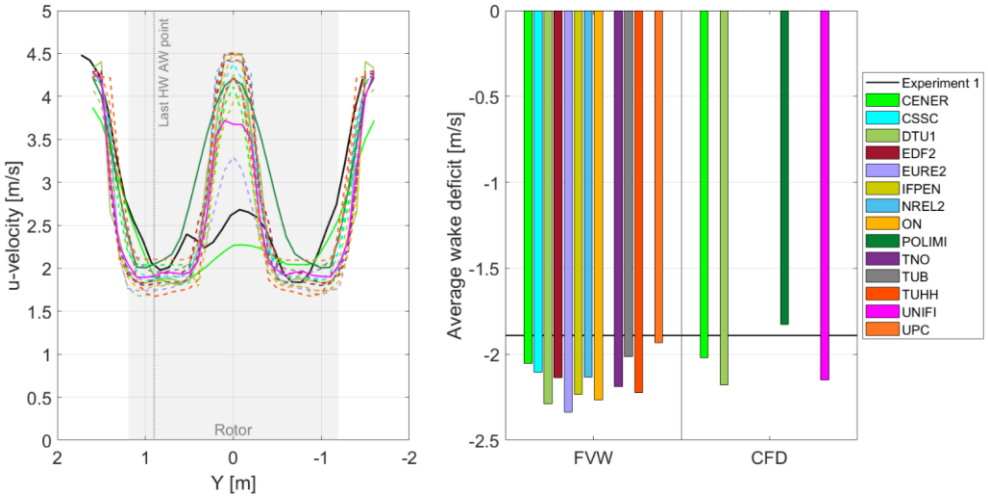

Figure 8: Left: Averaged hot-wire longitudinal velocity for one rotor revolution in the cross-wind direction (x = 5.48 m, z = hub height) during steady wind conditions. Right: Average wake deficit within the rotor region.

Figure 8 (right) shows the average wake deficit within the rotor region. Most participants tend to slightly overestimate the rotor average wake deficit. The average wake deficit (ΔU_{avg}) in a two-dimensional domain can be calculated in polar coordinates by means of Eq. (2):

$$\Delta U_{\text{avg}} = \frac{\int_0^{2\pi}\int_0^R r \cdot v(r,\theta) dr d\theta}{\pi R^2} \quad (2)$$

where R is the rotor radius, r is the radial distance from the origin, θ is the azimuth angle, and $v(r,\theta)$ is the wind deficit at a given location within the rotor region. The wind deficit in the longitudinal direction can be quantified by subtracting the incoming wind from the measured wind (u_{meas}) in the wake. See Eq. (3):

$$v(r,\theta) = u_{meas}(r,\theta) - U_0 \quad (3)$$

Formatted: Font: Italic
Formatted: Font: Italic
Formatted: Font: Italic
Formatted: Font: Italic
Formatted: Font: Italic
Formatted: Font: Italic
Formatted: Font: Italic
Formatted: Font: Italic
Formatted: Font: Italic
Formatted: Font: Italic
Formatted: Font: Italic
Formatted: Font: Italic
Formatted: Font: Italic

In this case, only the longitudinal wind velocities at some points along the y-direction are known. The average wake deficit in this one-dimensional discrete domain, equivalent to Eq. (2) in the continuous domain for an axisymmetric condition, can be computed by means of Eq. (4)~~.~~:

$$\Delta U_{\text{avg}} = \frac{\sum_{i=1}^{N} |r_i| \cdot v(r_i)}{\sum_{i=1}^{N} |r_i|} \quad (4)$$

where N denotes the number of points measured within the rotor region.

As ~~it~~ can be observed, Eq. (4) is weighted by the radial location. Accordingly, the relatively large differences between the experiment and the numerical models around y = 0 m due to the hub nose blockage do~~es~~ not have a significant impact.

5.1.3 PIV Measurements

For ~~the~~ E~~e~~xperiment 1, PIV measurements were taken during the steady wind condition. The longitudinal and vertical wind speeds as well as the vorticity magnitude about the y-direction were recorded at locations from x = 0.61 m to x = 1.36 m, and from z = 0.61 m to z = 1.4 m from the hub location with 5 mm increments in both directions. These velocity fields were measured~~recorded~~ at ~~given~~ times determined by the azimuth angle of one of the blades. The blade azimuth angles of interest were from 0 deg (blade pointing upwards) to 120 deg with a 15 deg step, and from 120 deg to 360 deg with a 30 deg step. Figure 9 (left) illustrates the location of this PIV plane behind the rotor. The location of this PIV plane can also be observed in Fig~~ure~~ 6. Figure 9 (right) shows ~~the~~an example of vorticity magnitude measured in the PIV plane during the experiment for the instant corresponding to the blade being at 30 deg azimuth. For the older vortex downstream, a reduction in vorticity magnitude as well as a less rounded shape due to the convection, diffusion and stretching of the vortex can be observed.

Formatted: Font: Italic
Formatted: Font: Italic
Formatted: Font: Italic
Formatted: Catalan
Formatted: Font: Italic
Formatted: Font: Italic
Formatted: Font: Italic
Formatted: Font: Italic
Formatted: Font: Italic

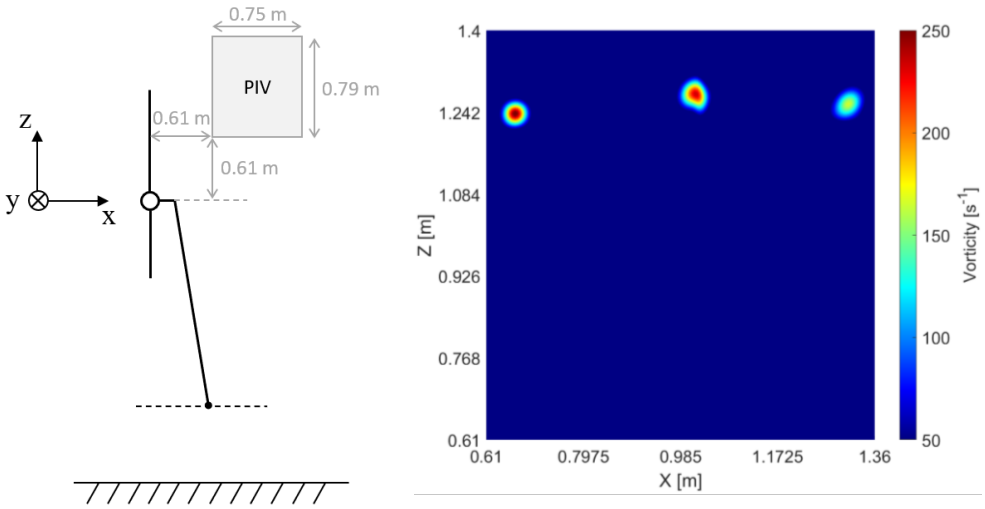

Figure 9: Left: Schematic representation of the wind turbine system and the PIV plane location. Right: Vorticity magnitude in the PIV plane during steady wind when blade azimuth location is 30 deg.

The scalar Gamma1 from Graftieaux's method (Graftieaux et al., 2001) was used for vortex tracking. Local maxima in the Gamma1 results were used to locate the centers of the blade tip vortices (Soto-Valle et al., 2022). The PIV plane records blade tip vortices from the three blades. Figure 10 shows the averaged blade tip vortex trajectory for the experiment and the participants using FVW (dashed) and CFD (solid) within the PIV plane. As expected, the tip vortex trajectories move outboard for increasing vortex age (i.e., when vortices~~ex~~ travel downwind). These tip vortex trajectories are representative of the wake expansion. Most numerical models tend to slightly overpredict the wake expansion. It is possible that the proximity of the blade tip to the ceiling in the experiments tends to inhibit a normal wake expansion (Soto-Valle et al., 2020). ~~Some participants using~~The CFD participants (e.g., POLIMI ~~UNIFI~~ and UNIFI~~POLIMI~~ in Fig. 10) that included the wind tunnel walls, floor, and ceiling, ~~showing~~obtained a better agreement with the experiment. FVW participants cannot include this boundary condition in their numerical models without implementing additional features. Interestingly, DTU1 (CFD) did not include the wind tunnel ceiling, and the wake expansion is aligned with the behavior observed by most FVW participants. A follow-on publication will focus on the hot-wire and PIV data to provide additional insights.

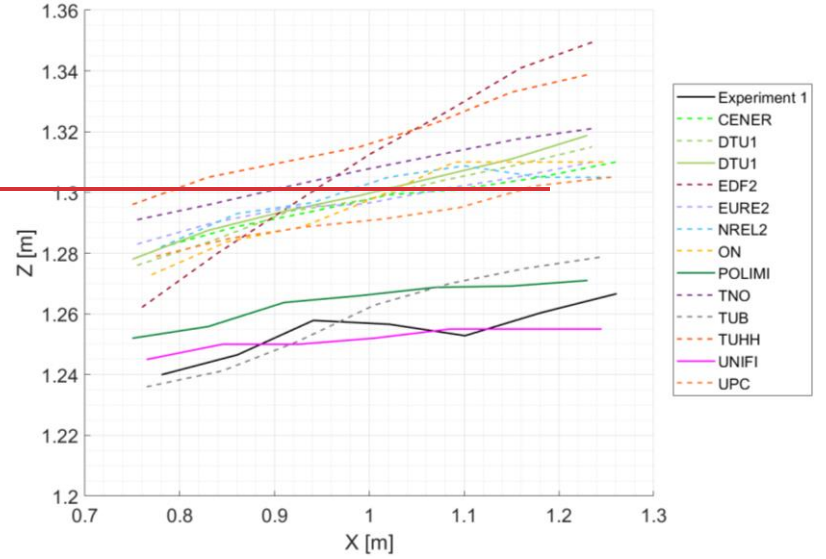
1.36
1.34
1.32
1.3
1.28
1.26
1.24
1.22
1.2
Z [m]
0.7
0.8
0.9
1
1.1
1.2
1.3
X [m]
Experiment 1
CENER
DTU1
DTU1
EDF2
EURE2
NREL2
ON
POLIMI
TNO
TUB
TUHH
UNIFI
UPC

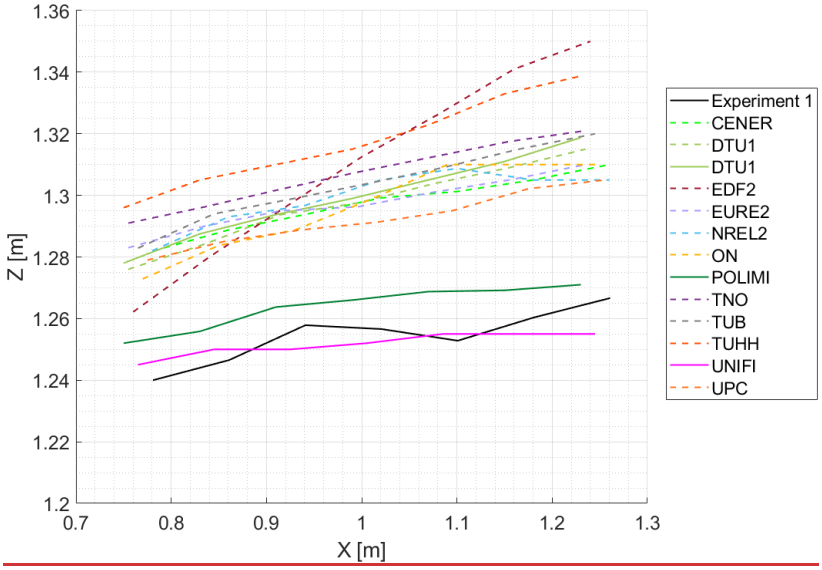
1.36
1.34
1.32
1.3
1.28
1.26
1.24
1.22
1.2
Z [m]
0.7
0.8
0.9
1
1.1
1.2
1.3
X [m]
Experiment 1
CENER
DTU1
DTU1
EDF2
EURE2
NREL2
ON
POLIMI
TNO
TUB
TUHH
UNIFI
UPC

Figure 10: Averaged blade tip vortex trajectory in the PIV plane during steady wind.

5.2 Unsteady Wind

The unsteady ~~wind~~ inflow conditions were achieved by means of forced harmonic motions. The system was studied under the same incoming wind as the steady wind condition but including different platform motion frequencies ($\omega = 2 \cdot \pi \cdot f$) and amplitudes ($A$). The platform displacement (x) is described according to Eq. (5) and the platform velocity ($\dot{x}$), stated by Eq. (6), is the time derivative of the platform displacement.:

$$x(t) = A \cdot sin(\omega \cdot t) \quad (5)$$

$$\dot{x}(t) = \omega \cdot A \cdot cos(\omega \cdot t) \quad (6)$$

The apparent wind experienced by the rotor is described by Eq. (7) and it is the combination of the incoming wind (U_0) and the platform velocity.:

$$w(t) = U_0 - \omega \cdot A \cdot cos(\omega \cdot t) \quad (7)$$

Figure 11 shows the platform displacement, platform velocity, and rotor apparent wind in angle domain for one platform period. Instead of using time in the x-axis, the platform motion phase is used.

Formatted: Font: Italic

Formatted: Font: Italic

Formatted: Font: Italic

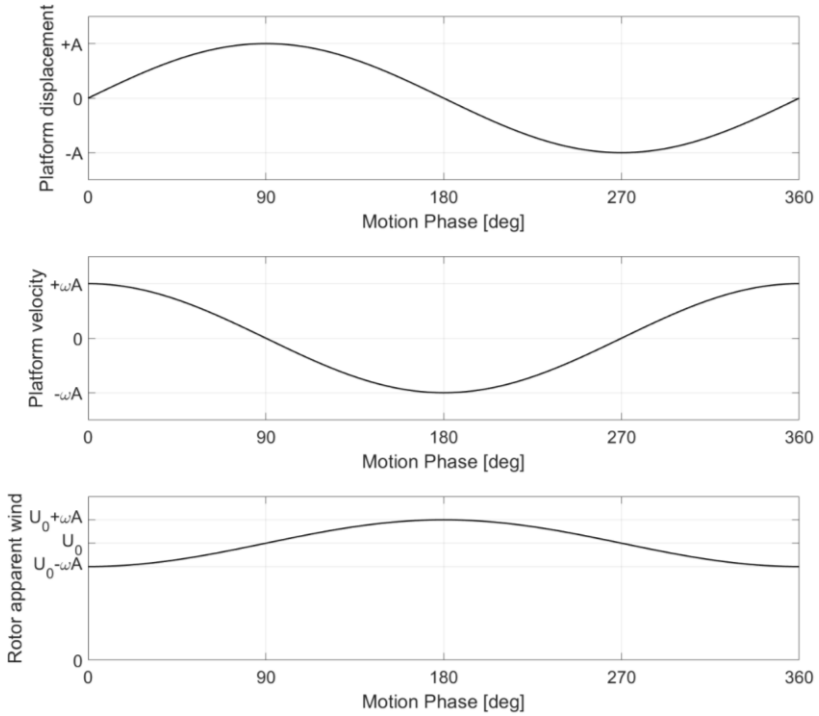

Figure 11: Platform displacement (top), platform velocity (middle), and rotor apparent wind (bottom) during one platform period.

For the surge motion, some participants kept the platform fixed and provided the rotor apparent wind as input wind in their simulations. This is a valid approach for the surge test if the rotor does not move into and out of its own wake, or the numerical model does not account for this potential interaction. Most participants kept the wind speed fixed and forced the motion of the wind turbine.

The rotor loads (e.g., thrust force and torque) are expected to follow the rotor apparent wind behavior (Figure 11 [bottom]). Figure 12 shows the expected relationship between the rotor loads and the platform displacement. A phase shift of 90 deg between the rotor loads and the platform displacement is expected for quasi-steady models. For example, BEM models with static polars should exhibit a phase shift of 90 deg.

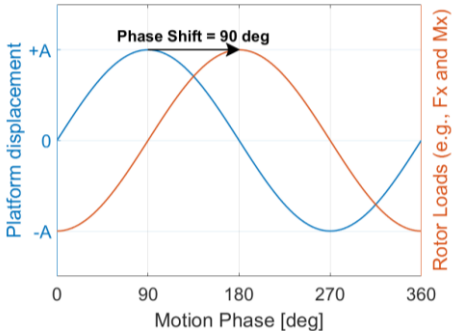

Figure 12: Expected relationship between rotor loads and platform displacement.

5.3 Unsteady Wind: Load Case 2.5

Load Cc~~a~~se 2.5 experiences the largest rotor apparent wind variation for the surge motion. The rotor loads are clearly driven by the platform motion, which translates into a good signal-to-noise ratio in the experiments.

The measured rotor loads were low-pass filtered with a 3 -Hz cut-off frequency, as mentioned in Section 4. This low-pass filter was performed in the frequency domain. The complex fast Fourier transform (FFT) was performed, the frequency of interest was kept (i.e., from 0 to 3 Hz), and the inverse of the FFT was applied to reconstruct the time domain signal. The main advantage of this approach is that it does not introduce a phase lag in the signal. For both experiments, the low-pass filtered rotor loads include ~~several~~around 15 surge periods, respectively. The loads were binned according to the platform motion and phase-averaged.

Figure 13 shows the aerodynamic thrust force from the two experiments and the participants. Different line styles are used to compare the different approaches. The participants using BEM are denoted with a dotted line, the ones using DBEM or GDW are denoted with a dashed-dotted line, the ones using FVW are denoted with a dashed line, and the CFD are denoted with a solid line. In the legend, participants using different modeling approaches appear with the line style associated with their highest model fidelity used.

The experiments primarily exhibit a first-order sine wave. This ~~denotes~~indicates that the response is driven by a single frequency (the platform motion). Overall, the mean value for ~~the~~ Ee~~x~~periment 1 and the participants is aligned with the value obtained during the steady case. For ~~the~~ Ee~~x~~periment 2, there is a small offset that could be due to the zero blade pitch recalibration performed during the testing campaign. For reference, the steady wind values obtained during both experiments have been included in the plot by means of two horizontal black dashed lines.

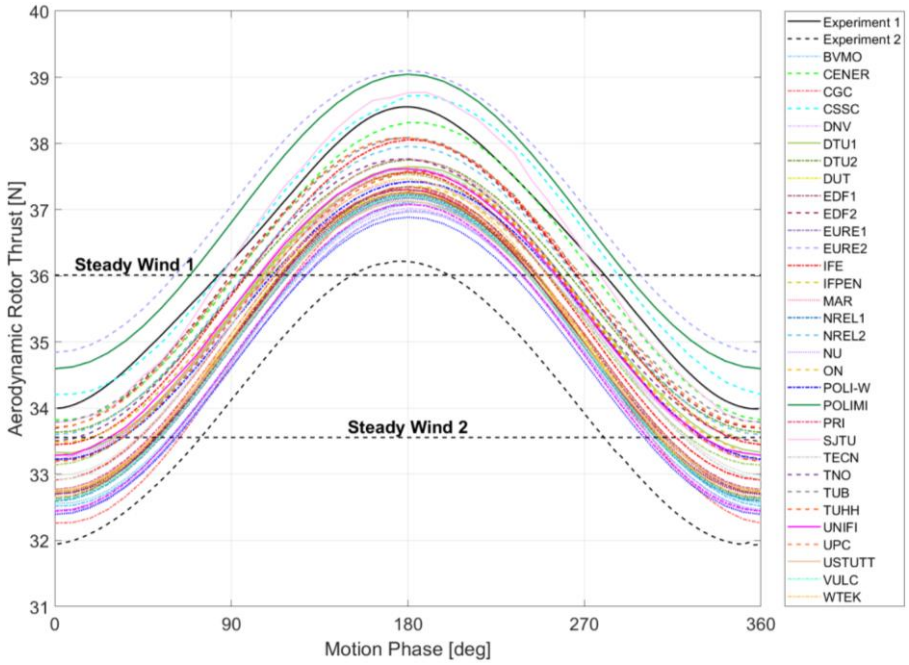

Figure 13: Aerodynamic rotor thrust variation during one surge period in Lload Ccase 2.5. Results from the experiments and participants. Pattern: BEM (:), DBEM (-.), GDW (-.), FVW (--), and CFD (-).

Figure 14 (left) shows the peak-to-peak amplitude of the aerodynamic rotor thrust. This peak-to-peak amplitude was computed as two times the FFT amplitude at the frequency of interest (e.g., 1 Hz corresponding to the platform motion in Lload Ccase 2.5). Interestingly, the participants using the same code with BEM and DBEM (i.e., BVMO, EDF, EURE, NREL, TECN, and VULC) return very similar values. The maximum difference observed within each participant between accounting or not accounting for dynamic inflow is 2.5 %. This indicates that the dynamic inflow does not have a significant impact in these conditions. Similarly, BEM or DBEM participants using the same code with static polars and unsteady airfoil aerodynamics (i.e., EDF, EURE, and NREL), show a maximum difference of 1 % in terms of peak-to-peak amplitude.

Formatted: English (United States)

Figure 14 (right) shows the phase shift between the aerodynamic rotor load and the platform motion. The phase angle was computed based on the real and imaginary part of the complex FFT at the frequency of interest. A red star is included if the numerical model uses static polars, a green star denotes models accounting for unsteady airfoil aerodynamics (UA), and a blue star indicates models using surface mesh. For the FVW solutions, part of the flow hysteresis is already accounted in the FVW theory. In this case, the solution is denoted as partial unsteady airfoil aerodynamics (greay star) if the participant used static

polars. As anticipated in Fig.~~ure~~ 12, the quasi-steady solutions (i.e., BEM with static polars) result in a phase shift at or very close to 90 deg. Most solutions including unsteady airfoil aerodynamics have phase shifts above 90 deg. This is due to a small hysteresis in airfoil performance undergoing angle of attack variations in attached flow (Theodorsen, 1935) rather than dynamic stall. The platform amplitudes and frequencies used in the experiment ensured that the dynamic stall was confined to the blade root (Fontanella et al., 2021b). The phase shift from most numerical models is aligned with the behavior observed in ~~the~~ Experiment 1. ~~The~~ Experiment 2 has a phase shift smaller than 90 deg that could be due to the impact of small rotor speed variations~~rotations~~ during the testing.

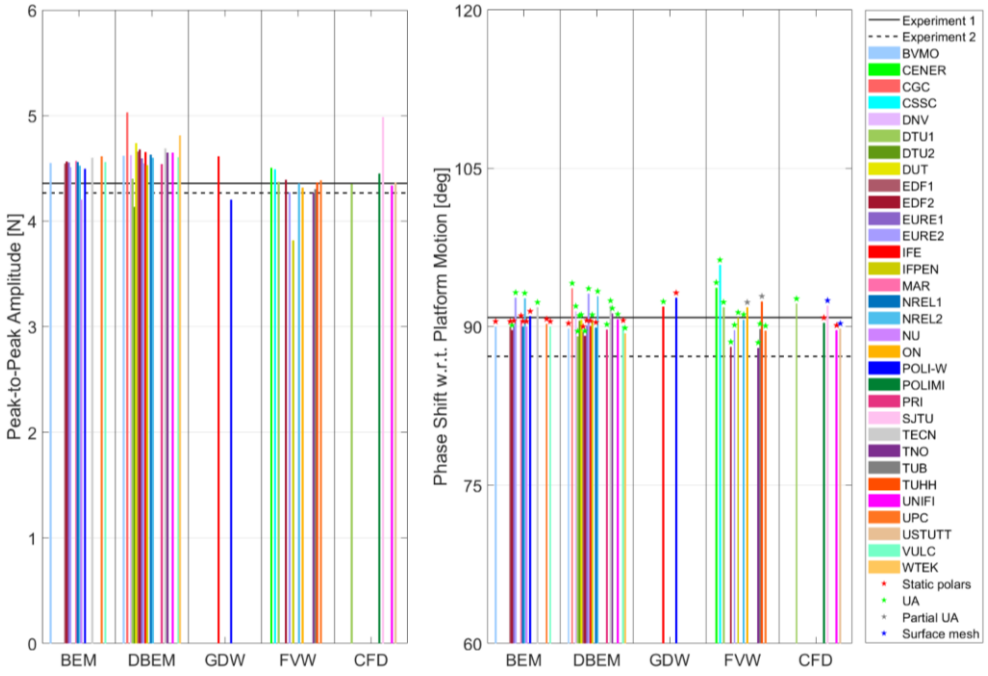

Figure 14: Aerodynamic rotor thrust peak-to-peak amplitude (left) and phase shift with regard to the platform motion (right) in Lload Ccase 2.5.

Figure 15 shows the lift coefficient versus angle of attack of the blade radial station 7 (42 % blade span) for one surge period during Lload Ccase 2.5. The output corresponds to two numerical models used by NREL with static polars (NREL1) and unsteady airfoil aerodynamics (NREL2). The static polar exhibits a constant slope as expected for the airfoil polar in the linear region; there is a unique relationship between the lift coefficient and the angle of attack. For the static polar, the lift coefficients when the platform moves from the 0 deg to 180 deg phase are symmetric to the coefficients when the platform moves from

the 180 deg to 360 deg phase. This implies that the response must be symmetric around the 180 deg motion phase if there is no other unsteadiness source (e.g., dynamic inflow). This symmetric behavior around ~~the~~ 180 deg can be observed for the quasi-steady solutions in Fig~~.ure~~ 13. When unsteady airfoil aerodynamics~~s~~ are considered, the lift coefficient describes a hysteresis loop. As Fig~~.ure~~ 15 shows, the lift coefficient when the platform moves from 0 to 180 deg is smaller compared to the platform moving from 180 to 360 deg. The response is not symmetric around the 180 deg motion anymore, resulting in a phase shift in rotor thrust slightly higher than 90 deg.

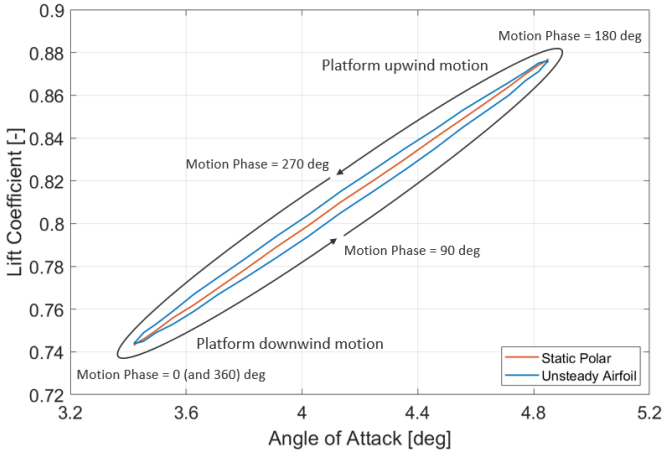

Figure 15: Lift coefficient versus angle of attack for a numerical model (NREL) using lifting line with static polars or unsteady airfoil aerodynamics.

Figure 16 shows the summarized aerodynamic rotor thrust and torque during one surge period. The figure shows the median for each modeling approach and the phase-averaged behavior from both experiments. The subindex next to each modeling approach indicates the number of results. As ~~it~~ can be observed, the aerodynamic rotor torque peak-to-peak amplitude in ~~the~~ Eexperiment 2 is lower than in ~~the~~ Eexperiment 1 (~12 %). There are no significant differences in terms of peak-to-peak amplitude or phase lag between the numerical models. The most remarkable difference is in terms of mean value for each modeling approach. In general, the mean value is ~~aligned~~consistent with the behavior observed during the steady wind condition (see Fig~~.ure~~ 5 for reference). Only the CFD approach seems to exhibit a slightly different mean value compared to the steady wind condition. As Fig~~.ure~~ 5 shows, the spread of the CFD participant outputs is significant. For ~~the~~ Lload Cc~~a~~se 2.5, only five out of seven CFD participants reported results. This can impact the mean value observed in Lload Cc~~a~~se 2.5 compared to the steady wind condition.

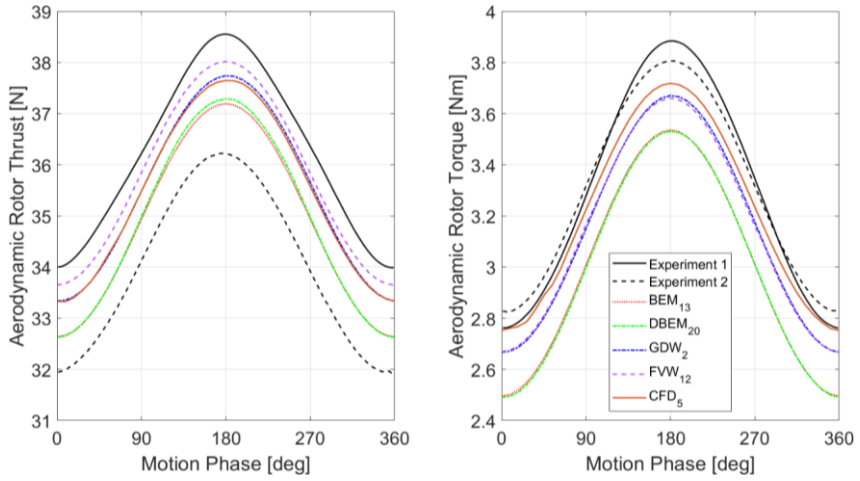

Figure 16: Aerodynamic rotor thrust and torque during the unsteady wind condition in Lload Ccase 2.5.

5.4 Unsteady Wind: Platform Motion Summary

The same analysis provided in Section 5.3 was performed for the different surge and pitch motions. The platform pitch motion results in a skewed flow due to the rotor plane tilt angle. In this case, there are aerodynamic loads in the different directions (e.g., ΔFx, ΔFy, ΔFz, ΔMx, ΔMy, ΔMz). However, the pitch amplitude is relatively small, and the amplitude of the loads different from thrust and torque (i.e., ΔFy, ΔFz, ΔMy, ΔMz) are very small. To compare the different conditions, the peak-to-peak amplitude of the aerodynamic rotor loads (ΔFx and ΔMx) were normalized according to the platform motion amplitude (A) in meters.

Figure 17 (left) shows the normalized aerodynamic rotor thrust variation for the different platform frequencies considered. The figure includes the results from both experiments and the median of the participants results (simulation, all modelling approaches considered) for the platform surge and pitch motions. The figure also includes the results from Lload Ccase 2.12 used for verification purposes.

A linear regression was also fitted to the simulation results and included in Fig.ure 17. As it can be observed, the simulation results lie on top of the linear regression for the frequency range studied. This confirms that the numerical models predict an aerodynamic rotor load variation that is linearly proportional to the changes in the rotor apparent wind, denoting a quasi-steady aerodynamic response. For example, increasing the platform motion amplitude or frequency by a factor of two would result in aerodynamic rotor load variations of the same order. This quasi-steady aerodynamic response is also alignedconsistent with the behavior observed in previous studies (Mancini et al., 2020; and Cormier et al., 2018). This behavior can also be verified by comparing the results from Lload Ccase 2.7 and Lload Ccase 2.12. These two load cases have the same platform frequency,

Formatted: Font: Italic
Formatted: Font: Italic
Formatted: Font: Italic
Formatted: Font: Italic
Formatted: Font: Italic
Formatted: Font: Italic
Formatted: Font: Italic
Formatted: Font: Italic
Formatted: Font: Italic

but different platform amplitudes. The platform amplitude in Lload Cease 2.12 was significantly increased from Lload Cease 2.7 to assess any potential unsteady aerodynamic response. When the aerodynamic rotor load is normalized by the platform amplitude, both load cases return the same value, confirming that there is no unsteady aerodynamic behavior. As expected, the linear regression shows zero variation of aerodynamic rotor loads at 0 Hz (i.e., no platform motion).

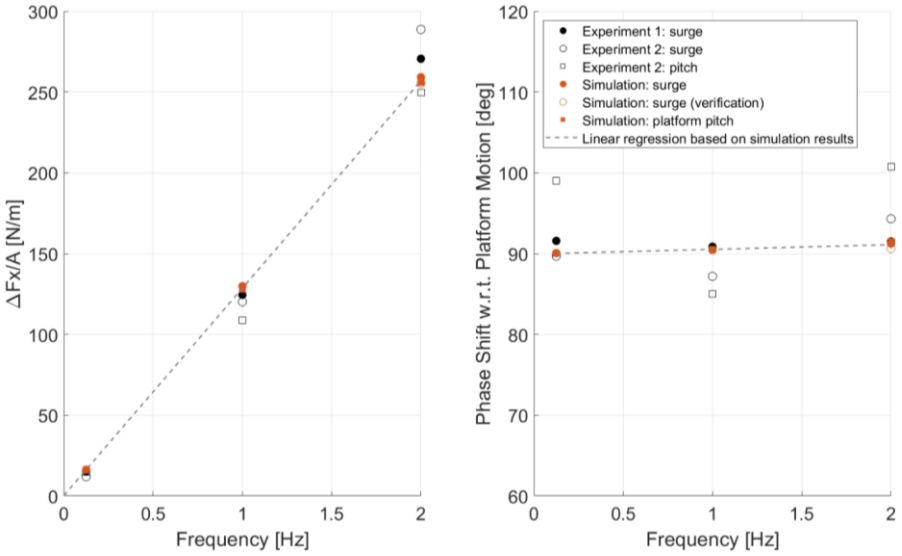

Figure 17: Normalized aerodynamic rotor thrust variation and phase shift with regard to platform motion during unsteady wind conditions, using Load Cases from 2.1 to 3.7 (excluding Load Cases 2.16 and 2.17).

The agreement between the numerical models and the experiments is good at the frequencies of 0.125 Hz and 1 Hz. No significant differences are observed between surge and the corresponding pitch motions. However, some dispersionspread is observed for the experiments at 2 Hz. This dispersion could come from the uncertainty associated to the inertial load subtraction from the measurements (Mancini et al., 2020).

Figure 17 (right) shows the phase shift of the aerodynamic rotor thrust with regardrespect to the platform motion. The numerical models predict a phase shift close to 90 deg at low frequencies (quasi-steady behavior) and a small increase with the frequency. This is mainly due to the small hysteresis in the airfoil aerodynamics in attached flow. The experiments show some dispersion, indicating that there is some uncertainty in the measurements. The results from the Eexperiment 1 show the closest behavior in terms of aerodynamic thrust variation and phase compared to the numerical models.

Figure 18 shows the equivalent information to Fig.ure 17, but in terms of aerodynamic rotor torque. Similar behavior as for the thrust force is observed. The main difference occurs for the aerodynamic torque variation at 2 Hz for the Eexperiment 1.

When looking in the frequency domain, the spectrum shows a significant amplitude at 2.5 Hz that could impact the system response during this testing condition and therefore the results should be used cautiously. This issue was also reported in Mancini et al.~~,~~ (2020). This unexpected frequency is not observed during ~~the~~ Eexperiment 2. ~~In this case~~For the aerodynamic rotor torque, the results from ~~the~~ Eexperiment 2 (surge motion) show the closest behavior in terms of aerodynamic torque variation and phase compared to the numerical models.

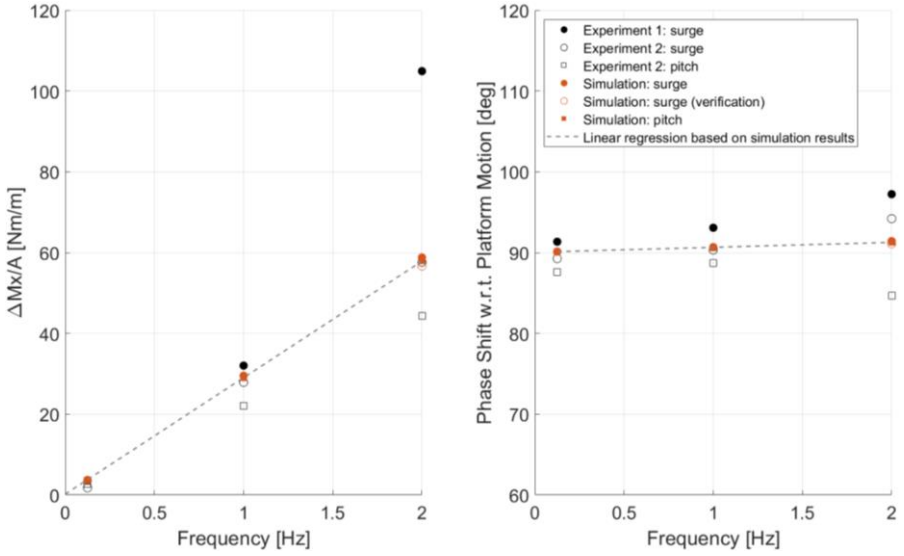

Figure 18: Normalized aerodynamic rotor torque variation and phase shift with regard to platform motion during unsteady wind conditions, using Load Cases from 2.1 to 3.7 (excluding Load Cases 2.16 and 2.17).

5.5 Unsteady Wind: Rotor Speed and Blade Pitch V~~v~~ariations

During both experiments, the rotor speed and blade pitch angle were held constant. However, in real wind turbine operating conditions, platform surge and pitch variations would result in rotor speed variations and blade pitch actuations.

Modern variable~~-~~speed wind turbines use generator torque control and blade pitch angle control. Below rated power, the blades are kept at the minimum (optimal) blade pitch angle setting and the wind turbine is governed by the generator torque. In this region, rotor torque changes due to unsteady wind conditions will lead to rotor speed variations. When the wind turbine is operating at rated power, the blade pitch angle is used to keep the wind turbine rotor at a constant speed and producing the desired power. In this region, the blade pitch angle needs to vary to keep the rotor torque constant. Near the rated power

condition, the controller can be transitioning between the generator torque and blade pitch control. In this region, there could be rotor speed and blade pitch variations.

To illustrate the impacts that the wind turbine controller could have over the system loading, verification Lload Cases 2.16 and 2.17 were included in the study (with no corresponding experimental measurements for validation). These two load cases use the platform motion from Lload Case 2.12 as a baseline. The proposed rotor speed and blade pitch variations follow the same behavior as the aerodynamic rotor torque (i.e., they are governed by the rotor apparent wind). Equation (8) describes the rotor speed (Ω) in revolutions per minute in Lload Case 2.16 and Eq. (9) describes the blade pitch angle (β) in deg in Lload Case 2.17. The proposed rotor speed and blade pitch variations are based on values observed in similar FOWT studies (Ramos-García et al., 2022). Under these conditions, dynamic stall is confined to the blade root like for the previous load cases analyzed.

$$\Omega(t) = 240 - 36 \cdot cos(\omega \cdot t) \quad \text{(Load Case 2.16)} \tag{8}$$

$$\beta(t) = 1.5 - 1.5 \cdot cos(\omega \cdot t) \quad \text{(Load Case 2.17)} \tag{9}$$

The rotor speed and blade pitch angle are imposed assuming that there are no system dynamics involved. In real conditions, the rotor would speed up or slow down at a rate that depends on the system rotational inertia and the generator resistive torque curve. Regardless, the imposed motions should be reasonably representative.

Figure 19 (left) shows the aerodynamic rotor thrust peak-to-peak amplitude for the different participants and the median for each modeling approach in Lload Case 2.16 (platform motion and rotor speed variation). Interestingly, the modeling approaches including dynamic inflow (DBEM, GDW, FVW, and CFD) predict similar values while the BEM solution predicts a lower value. Figure 19 (right) shows the phase shift with regard to the platform motion. Similar behavior is observed for the aerodynamic rotor torque (not shown).

Formatted: Font: Italic

Formatted: Font: Italic

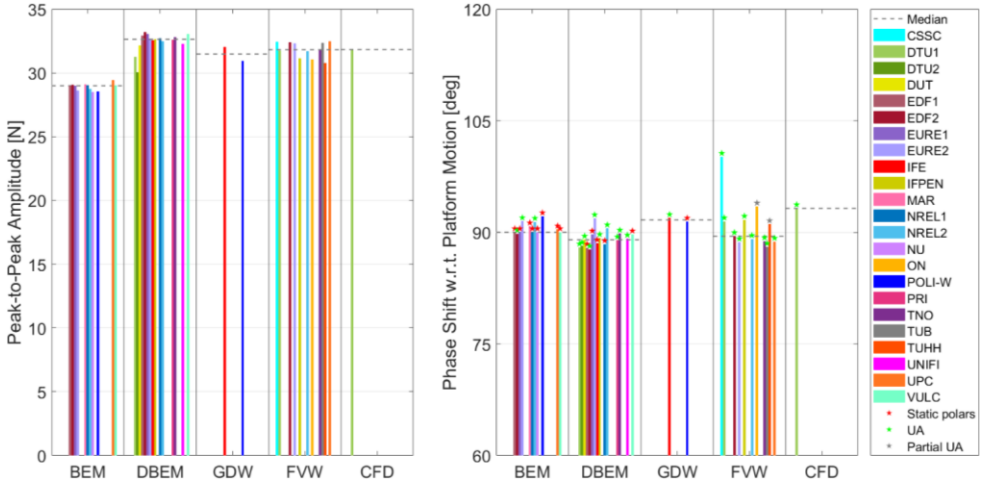

Figure 19: Aerodynamic rotor thrust peak-to-peak amplitude (left) and phase shift with regard to the platform motion (right) in Lload Ccase 2.16.

Figure 20 shows a summary of the results by modeling approach for ~~the~~ Lload Ccases 2.12, 2.16, and 2.17. Figure 20 (left) shows the aerodynamic rotor thrust peak-to-peak amplitude. For ~~the~~ Lload Ccase 2.16, the output is equivalent to the one shown in Fig.~~ure~~ 19. The peak-to-peak amplitude in Lload Ccase 2.16 is significantly larger than in Lload Ccase 2.12 due to the rotor speed oscillations. The blade pitch actuation in Lload Ccase 2.17 alleviates the rotor loading variations as intended by the wind turbine controller, resulting in smaller peak-to-peak amplitudes compared to Lload Ccase 2.12.

There is good agreement between modeling approaches when only the platform motion is considered (Lload Ccase 2.12). The maximum difference between any approach and the average of all modeling approaches is within 3 %. However, when there is platform motion and rotor speed variations (Lload Ccase 2.16), not accounting for dynamic inflow (i.e., BEM approach) results in load variation amplitudes that are 9 % lower compared to the average of the solutions that account for dynamic inflow effects (DBEM, GDW, FVW, and CFD). When there is platform motion and blade pitch actuations (Lload Ccase 2.17), not accounting for dynamic inflow results in load variation amplitudes that are 18 % higher.

The dynamic inflow effect for sudden blade pitch angle changes (e.g., step changes) is well known (Snel and Schepers, 1995). For sudden actuations, relevant dynamic overshoot loads compared to quasi-steady calculations are expected. Interestingly, for the blade pitch and platform harmonic motion considered here (Load Case 2.17), the dynamic inflow results in smaller peak-to-peak variations.

Figure 20 (right) shows the phase shift of the aerodynamic thrust with regard to the platform motion by modeling approach. For the BEM and DBEM approaches, a red star denotes the median solution for the models using static polars, and a green

star is used for the median solution of the models using unsteady airfoil aerodynamics. As expected, the BEM approaches with static polars show a phase shift of 90 deg regardless of the ~~boundary~~operating conditions. The use of unsteady airfoil aerodynamics in BEM or DBEM returns phase shifts that are slightly higher compared to the static polars. The effect of the dynamic inflow in the phase shift can be observed in L~~l~~oad C~~c~~ases 2.16 and 2.17. In L~~l~~oad C~~c~~ase 2.16, the phase shift slightly decreases compared to L~~l~~oad C~~c~~ase 2.12, while the phase shift in L~~l~~oad C~~c~~ase 2.17 slightly increases. Despite these variations, the phase shift remains close to the expected 90 deg with a maximum difference smaller than 10 deg.

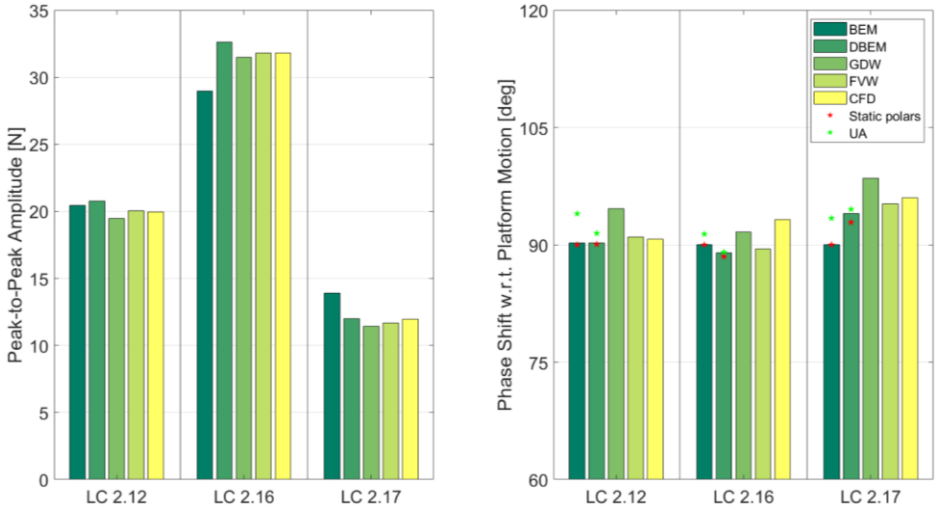

Figure 20: Left: Aerodynamic rotor thrust peak-to-peak amplitude in L~~l~~oad C~~c~~ase (LC) 2.12 (constant rotor speed and blade pitch), 2.16 (varying rotor speed), and 2.17 (varying blade pitch). Right: Phase shift with regard to the platform motion.

6 Conclusions

In the frame of the OC6 Phase III project, participants modeled a scaled version of the DTU 10 -MW RWT and studied the system response under steady and unsteady wind conditions. The results of numerical models with different fidelity levels were compared against two testing campaigns performed at Politecnico di Milano for platform surge and pitch harmonic motions. Good agreement was observed between the numerical models and the experiments for the platform frequencies and amplitudes considered. For reference, these tests correspond to periods between 12.5 and 200 s~~econds~~ at full- scale and nacelle motion amplitudes between 0.6 and 9.375 m~~eters~~. No significant differences between the numerical models of different fidelity were observed during the forced platform motions. For these tests, the aerodynamic rotor load was linearly proportional to the rotor apparent wind, denoting a quasi-steady aerodynamic response. Only a small hysteresis in airfoil performance undergoing

angle of attack variations in attached flow was observed by participants using unsteady airfoil aerodynamics. This introduced a small phase shift in the rotor loads, but the impact was limited.

Additional load cases were also included to understand if other conditions could produce a significant unsteady aerodynamic behavior. It was observed that the change in the flow conditions due to rotor speed and blade pitch variations combined with the platform motion resulted in such unsteady aerodynamic response. While there were no measurement data available for these conditions, the numerical models showed significant differences based on the modeling approach used. Those that d~~o~~id not include dynamic inflow effects predicted rotor load variation amplitudes 9 % smaller under rotor speed variations and load variation amplitudes 18 % higher when there were blade pitch actuations. The dynamic inflow also had limited impact on the phase of the rotor loads. Thus, this work has shown that while the motion of the turbine itself does not require an unsteady aerodynamic modeling approach to accurately predict the loads in the turbine (at least for the design and forced motion studied in this project), a realistic condition where generator torque control and blade pitch angle control is included will need unsteady aerodynamic models (both airfoil unsteady aerodynamics and dynamic inflow models) for accurate load prediction.

Data Availability

The modeling information, the simulation results, and the experimental data from this project will be made available to the public by the end of 2022 through the U.S. Department of Energy Data Archive and Portal, https://a2e.energy.gov/projects/oc6. The data set developed during the UNAFLOW project is available at Fontanella et al.~~,~~ (2021a).

Author Contributions

Alessandro Fontanella, Marco Belloli, Paolo Schito, Alberto Zasso, Giacomo Persico, and Andrea Sanvito: Planned and performed the measurements in both experimental campaigns. Amy Robertson: Secured the funding for the OC6 project. Roger Bergua, Amy Robertson, and Jason Jonkman: Proposed the methodology, formal analysis, and investigation. All authors from institutions 1-2 and 4-3~~1~~0: Simulated the system and submitted results from their numerical models (detailed in Section 3). Roger Bergua: Postprocessed and visualized the data from the experiments and the numerical models. Rodrigo Soto-Valle and Stefano Cioni: Postprocessed the PIV data to obtain the tip vortex trajectory. Roger Bergua: Wrote the manuscript draft. All authors: Reviewed and edited the manuscript.

Competing Interests

Some authors are members of the editorial board of Wind Energy Science journal. The peer-review process was guided by an independent editor, and the authors have also no other competing interests to declare.

Acknowledgements

The authors would like to thank Politecnico di Milano for providing the data to characterize the numerical models, the data recorded during the UNAFLOW and the follow-on campaigns, as well as for their ongoing support.

This work was authored in part by the National Renewable Energy Laboratory, operated by Alliance for Sustainable Energy, LLC, for the U.S. Department of Energy (DOE) under Contract No. DE-AC36-08GO28308. Funding was provided by the U.S. Department of Energy Office of Energy Efficiency and Renewable Energy Wind Energy Technologies Office. The views expressed in the article do not necessarily represent the views of the DOE or the U.S. Government. The U.S. Government retains and the publisher, by accepting the article for publication, acknowledges that the U.S. Government retains a nonexclusive, paid-up, irrevocable, worldwide license to publish or reproduce the published form of this work, or allow others to do so, for U.S. Government purposes.

References

Bak, C., Zahle, F., Bitsche, R., Kim, T., Yde, A., Henriksen, L.C., Hansen, M. H., Blasques, J.P., Gaunaa, M., and Natarajan A. The DTU 10-MW reference wind turbine. In Danish wind power research, 2013.

Bayati, I., Belloli, M., Bernini, L., and Zasso, A. Wind tunnel wake measurements of floating offshore wind turbines. Energy Procedia 137: 214-222, https://doi.org/10.1016/j.egypro.2017.10.375, 2017.

Bayati, I., Belloli, M., Bernini, L., Boldrin, D. M., Boorsma, K., Caboni, M., Cormier, M., Mikkelsen, R., Lutz, T., and Zasso, A. UNAFLOW project: UNsteady aerodynamics of FLOating wind turbines. J. Phys.: Conf. Ser. 1037 072037. doi: https://doi.org/10.1088/1742-6596/1037/7/072037, 2018.

Cormier, M., Caboni, M., Lutz, T., Boorsma, K., and Krämer, E.: Numerical analysis of unsteady aerodynamics of floating offshore wind turbines, J. Phys.: Conf. Ser. 1037 072048, https://doi.org/10.1088/1742-6596/1037/7/072048, 2018.

Ferreira, C., Yu, W., Sala, A., and Viré, A.: Dynamic inflow model for a floating horizontal axis wind turbine in surge motion, Wind Energ. Sci., 7, 469–485, https://doi.org/10.5194/wes-7-469-2022, 2022.

Fontanella, A., Bayati, I., Mikkelsen, R., Belloli, M., and Zasso, A.: UNAFLOW: UNsteady Aerodynamics of FLOating Wind turbines, Zenodo [data set], https://doi.org/10.5281/zenodo.4740006, 2021a.

Fontanella, A., Bayati, I., Mikkelsen, R., Belloli, M., and Zasso, A.: UNAFLOW: a holistic wind tunnel experiment about the aerodynamic response of floating wind turbines under imposed surge motion, Wind Energ. Sci., 6, 1169–1190, https://doi.org/10.5194/wes-6-1169-2021, 2021b.

Graftieaux, L., Michard, M., and Grosjean, N.: Combining PIV, POD and vortex identification algorithms for the study of unsteady turbulent swirling flows, Meas. Sci. Technol. 12 1422, https://doi.org/10.1088/0957-0233/12/9/307, 2001.

International Energy Agency Wind Technology Collaboration Programme (IEA Wind) Task 30. Available online: https://www.iea-wind.org/task30/, last access: 17 May 2022.

Li, A., Gaunaa, M., Pirrung, G. R., Meyer Forsting, A., and Horcas, S. G.: How should the lift and drag forces be calculated from 2-D airfoil data for dihedral or coned wind turbine blades?, Wind Energ. Sci., 7, 1341–1365, https://doi.org/10.5194/wes-7-1341-2022, 2022.

Mancini, S.: An Experimental, Analytical and Numerical Study of FOWT's Unsteady Aerodynamics, MS thesis, Politecnico di Milano, Milan, Italy, 2020.

Mancini, S., Boorsma, K., Caboni, M., Cormier, M., Lutz, T., Schito, P., and Zasso, A.: Characterization of the unsteady aerodynamic response of a floating offshore wind turbine to surge motion, Wind Energ. Sci., 5, 1713–1730, https://doi.org/10.5194/wes-5-1713-2020, 2020.

Ramos-García, N., Kontos, S., Pegalajar-Jurado, A., González Horcas, S., and Bredmose, H.: Investigation of the floating IEA Wind 15 MW RWT using vortex methods Part I: Flow regimes and wake recovery, Wind Energ., https://doi.org/10.1002/we.2682, 2022.

Robertson A., Bergua R., Fontanella A., Jonkman J. OC6 Phasde III Definition Document (NREL/TP-5000-83102). National Renewable Energy Laboratory (NREL), Golden, CO (United States). 2022.

Snel, H., and J. G. Schepers.: Joint investigation of dynamic inflow effects and implementation of an engineering method, 1995.

Soto-Valle, R., Alber, J., Manolesos, M., Nayeri, C. N., and Paschereit, C. O.: Wind turbine tip vortices under the influence of wind tunnel blockage effects, J. Phys. Conf. Ser. 1618 032045, https://doi.org/10.1088/1742-6596/1618/3/032045, 2020.

Soto-Valle, R., Cioni, S., Bartholomay, S., Manolesos, M., Nayeri, C. N., Bianchini, A., and Paschereit, C. O.: Vortex identification methods applied to wind turbine tip vortices, Wind Energ. Sci., 7, 585–602, https://doi.org/10.5194/wes-7-585-2022, 2022.

Theodorsen, T.: General Theory of Aerodynamic Instability and the Mechanism of Flutter, Technical Report NACA TR-496, NACA, 1935.

Veers, P., Bottasso, C., Manuel, L., Naughton, J., Pao, L., Paquette, J., Robertson, A., Robinson, M., Ananthan, S., Barlas, A., Bianchini, A., Bredmose, H., Horcas, S. G., Keller, J., Madsen, H. A., Manwell, J., Moriarty, P., Nolet, S., and Rinker, J.: Grand Challenges in the Design, Manufacture, and Operation of Future Wind Turbine Systems, Wind Energ. Sci. Discuss. [preprint], https://doi.org/10.5194/wes-2022-32, in review, 2022.